CHALMERS
UNIVERSITY OF TECHNOLOGY

CFD Analysis of a Low-Pressure Turbine for Evaluating High-Temperature NOx Emission Control Catalysts in Turbofan Engines

Master's thesis in Mobility Engineering MMSX30, Aerospace track

ANTON FORSLER
MATIAS LEMA

CHALMERS UNIVERSITY OF TECHNOLOGY
Gothenburg, Sweden 2026
www.chalmers.se

MASTER'S THESIS 2026

CFD Analysis of a Low-Pressure Turbine for Evaluating High-Temperature NOx Emission Control Catalysts in Turbofan Engines

A Master's Thesis in Mobility Engineering

Anton Forsler
Matias Lema

CHALMERS
UNIVERSITY OF TECHNOLOGY

Department of Mechanical Engineering
Division of Fluid Dynamics
CHALMERS UNIVERSITY OF TECHNOLOGY
Gothenburg, Sweden 2026

CFD Analysis of a Low-Pressure Turbine for Evaluating High-Temperature NOx Emission Control Catalysts in Turbofan Engines
A Master's Thesis in Mobility Engineering MMSX30
Anton Forsler
Matias Lema

Supervisors: Joakim Halldin Stenlid, Department of Chemistry and Chemical Engineering
Patrick Donald Sinko, Department of Life Sciences
Examiner: Valery Chernoray, Department of Mechanical Engineering

Master's Thesis 2026
Department Mechanical Engineering
Division of Fluid Dynamics
Chalmers University of Technology
SE-412 96 Gothenburg
Telephone +46 31 772 1000

Cover: Render of the Low Pressure Turbine.

Typeset in LaTeX
Printed by Chalmers Reproservice
Gothenburg, Sweden 2026

CFD Analysis of a Low-Pressure Turbine for Evaluating High-Temperature NOx Emission Control Catalysts in Turbofan Engines
A Master's Thesis in Mobility Engineering
Anton Forsler
Matias Lema
Department of Mechanical Engineering
Chalmers University of Technology

Abstract

Emissions from aviation are a pressing topic today, and nitrogen oxides are among the most harmful emissions produced by turbofan engines. Tighter controls on NOx emissions are likely to become increasingly important, and reducing these emissions will be a key challenge in the coming years. Even under current regulations, significantly decreasing NOx without a performance penalty at a given design point could enable new high-efficiency engine designs.
The common solution for NOx reduction in other industries is a catalytic converter. However, such a device would incur severe performance losses in a turbofan engine and present major durability challenges due to the hostile operating environment.
This thesis investigates the novel possibility of coating the internal surfaces of the low-pressure turbine of a turbofan engine with a durable catalytic alloy that acts as an integrated, albeit less efficient, catalytic converter. Building on previous work and in collaboration with NASA, a coupled model combining computational fluid dynamics and surface chemistry in 2D and was used to evaluate NOx conversion over a stator row in the first stage of the low-pressure turbine of the NASA E3 engine and lay the groundwork for 3D simulations. The aim was to assess the concept and provide an initial proof of principle for its viability. Several RANS models were used for flow simulations in COMSOL, culminating in a compressible $k^{\omega}\omega$ model and coupled chemistry was modelled using Chalmers catalyst data. The results suggest that further work is warranted and that integrated catalytic turbine surfaces represent a promising avenue for NOx reduction in aviation.

Keywords: Low pressure turbine, Catalysis, CFD, RANS, E^3 engine

Acknowledgements

I would like to thank my family and friends for the unending support during my studies in Portugal and Sweden. A special thank you to Mangas and Erik for welcoming me to Sweden and motivating me to embark on this journey.

Matias

I would like to thank my family for all the help and support they have given me throughout the duration of this thesis as well as during my time at Chalmers as a whole. I would also like say thank you to my friends whom I've gotten to know during my time at Chalmers.

Anton

We would both like to thank the team at NASA and our examiner Valery Chernoray for the support and for making this thesis possible. A special thanks to our supervisors Joakim Halldin Stenlid and Patrick Donald Sinko for all their help with COMSOL, chemistry as a whole, and for making us feel at home in this department. We would also like to thank Scott Sherriff for his work on the chemistry models and being a great colleague.

Gothenburg, June, 2026

List of Acronyms

Below is the list of acronyms that have been used throughout this thesis listed in alphabetical order:

BPR Bypass ratio
CAD Computer aided design
CFD Computational fluid dynamics
CPU Central processing unit
DNS Direct Numerical Simulation
FEM Finite element method
FVM Finite volume method
GCI Grid convergence index
HPC High pressure compressor
HPT High pressure turbine
LES Large eddy simulation
LPC Low pressure compressor
LPT Low pressure turbine
LTO Landing and Take-off
NOx Nitrogen oxides
OPR Overall pressure ratio
PDE Partial differential equation
RAM Random access memory
RANS Reynolds-averaged Navier-Stokes
SFC Specific fuel consumption
SSH Secure Shell
TDS Transport of diluted species
TKE Turbulent kinetic energy
TOF Turnover frequency
WALE Wall-adapting Local Eddy-viscocity

Nomenclature

Below is the nomenclature of indices, sets, parameters, and variables that have been used throughout this thesis.

Compressible flow

M	Mach number
a	Speed of sound
ρ	Density
T_n	Static temperature at n
T_{0n}	Total temperature at n
p_n	Static pressure at n
p_{0n}	Total pressure at n
R	Specific gas constant
γ	Heat capacity ratio
C_p	Specific heat capacity
$\dot{m}$	Mass flow

Turbofans

U	Axial velocity
M_{ax}	Axial Mach number
h	Blade height
r_{tip}	Radius at blade tip
r_{hub}	Radius at blade hub
r_{mid}	Radius at mid blade length
F_N	Net thrust

Turbulence and CFD

ν	Kinematic viscosity
k	Turbulent kinetic energy
ϵ	Turbulence dissipation rate
ω	Specific turbulence dissipation rate
l_0	Integral length scale
η	Kolmogorov length scale
C_μ	Turbulent flow constant
Δ	Mesh cell length

Chemistry

N_A	Avogadro's constant
Γ	Surface molar site density
c_i	Molar concentration for species i
$r_{i,vol}$	Volumetric consumption rate for species i
ρ_i	density of species i
M_i	Molar mass of species i
J_i	Local wall flux of species i
N_i	Molar flux of species i

Contents

List of Acronyms ix

Nomenclature xi

List of Figures xv

List of Tables xvii

1 Introduction 1
- 1.1 Background . . . 1
- 1.2 Turbofans . . . 1
- 1.3 NOx . . . 2
- 1.4 Catalyst . . . 2
- 1.5 Main Goals . . . 3
- 1.6 Limitations . . . 4
- 1.7 Ecological and Environmental Objectives . . . 4

2 Theory 7
- 2.1 Turbulence . . . 7
- 2.2 CFD . . . 8
  - 2.2.1 Navier-Stokes Equations . . . 9
- 2.3 RANS . . . 9
  - 2.3.1 RANS EVM . . . 9
  - 2.3.2 $K-\epsilon$ . . . 10
  - 2.3.3 $K-\omega$ . . . 10
- 2.4 LES . . . 10
- 2.5 Chemistry for Catalytic NOx Reduction . . . 11
  - 2.5.1 Microkinetic Model . . . 11
  - 2.5.2 Active Site Density & Turnover Frequency . . . 11
  - 2.5.3 Species Transportation . . . 12

3 Methods 13
- 3.1 2D Geometry . . . 13
- 3.2 Meshing and Numerical Setup - 2D RANS . . . 14
  - 3.2.1 Mesh Refinement . . . 16
  - 3.2.2 Numerical Setup . . . 16
- 3.3 3D Geometry . . . 17

3.4 Meshing and Numerical Setup - 3D RANS 19
3.4.1 Meshing 19
3.4.2 Numerical Setup 19
3.5 Mesh Refinement for LES 20
3.6 Numerical Setup - LES 21
3.7 Chemistry Implementation 21
3.8 Validation and GCI 23

4 Results & Discussion **25**
4.1 Preliminary 2D Runs 25
4.2 2D GCI 26
4.3 2D Validation 27
4.4 2D Flow Results 29
4.5 2D Runs with Chemistry Coupling 34
4.6 NOx Conversion Measurement Inadequacy 35
4.6.1 Alternative NO_X Conversion Measurement Method and Partial Pressures 38
4.7 Preliminary 3D Runs 39
4.7.1 Special Considerations with Meshing 39
4.7.2 Sweeping Velocity Inlet Conditions Around A Center of Rotation 40
4.7.3 Convergence Issues 42
4.8 High Performance Computing Cluster, Vera 43

5 Future work **45**
5.1 CFD Recommendations 45
5.2 Surface Chemistry Recommendations 46

6 Conclusion **47**

7 Declaration of AI use **49**

Bibliography **51**

A Appendix **I**

List of Figures

2.1 The different length scales in a turbulent energy cascade 7

3.1 Pitch-line highlighted in original NASA first stator geometry 14
3.2 Flattened Pitch-lines arrayed in finalized 2D geometry 14
3.3 Initial 2D mesh 15
3.4 Detail 1 15
3.5 Detail 2 15
3.6 Added detail along exit flow angles 15
3.7 Refined Boundary slayers 16
3.8 Further wake region refinement 16
3.9 Highlighted domain that was simulated in 3D with the vane that was included in red 18
3.10 Final 3D geometry with hub and casing in gray, stator in red, and glass representing the fluid domain 19
3.11 Example of size of eddies vs mesh size required to resolve them . 20

4.1 Areas with $f_{fineness} < 5$ 25
4.2 closeup 25
4.3 Closeup of areas with $f_{fineness} < 5$ after wake refinement 26
4.4 Total pressure across domain at cruise 28
4.5 Velocity flow angle at stator outlet 28
4.6 Mach Number distribution around the stator. Blue line and red dots are from [1], while green line and black dots are from the COMSOL cruise simulation 29
4.7 Velocity throughout domain 30
4.8 Streamlines around stators 30
4.9 Static pressure across domain 30
4.10 Total pressure across domain 30
4.11 Static temperature across domain 31
4.12 Density across domain 32
4.13 Mach number at stator outlet 33
4.14 Change in NO molar concentration X_{NO} across domain in the units mol/m^3, arrows display NO molar flux. 34
4.15 $\%X_{NO}$ of time dependent study, displaying a 14.786% conversion . 35
4.16 Zoomed in $\%\rho$ (in green) and $\%X_{NO}$ (in blue) over simulation time 36
4.17 $\%X_{NO}$ plot from the previous work (stabilizes at 0.036%) 37

4.18 $\%N_{NO}$ plot from same results (stabilizes at same values and behaves the exact same) . . . 37
4.19 NO conversion in molar flux ($\%N_{NO}$) . . . 38
4.20 Closeup of the early casing mesh with casing-periodic edges in blue 39
4.21 Closeup of a later 3D mesh cut at $x = 25$mm showing stator and casing boundary layer connection (periodic boundary in red) . . . 40
4.22 Interpolated axial velocity field . . . 41
4.23 Axial velocity with boundary layers . . . 41
4.24 Early inlet setup in COMSOL (axial velocity field U_{nasa} and radial velocity field V_{nasa}) . . . 41
4.25 Curved banding in inlet suggests the setup is working as intended 41
4.26 Inlet velocity field with accurate velocity directions but vector length increased to aid visualization . . . 42
4.27 Typical COMSOL batch job performance without meshing . . . 43
4.28 Performance for a job that included meshing (meshing from around 14:05:30 to 14:08:30) . . . 44

A.1 Schematic of the E^3 engine from "Energy efficient engine - flight propulsion system final design and analysis" [2] . . . I
A.2 Schematic of the E^3 LPT from "Energy efficient engine - flight propulsion system final design and analysis" [2] . . . II
A.3 3D geometry in blender quad mesh (viewed from the inlet) . . . III
A.4 HPT outlet excel sheet data . . . IV
A.5 Example of bash script used for running COMSOL on Vera . . . V
A.6 Isentropic Mach Number distribution around each stator from the E^3 LPT performance report [1] calculated from static pressure taps VI
A.7 Outlet swirl angle after the first stator row from the E^3 LPT performance report [1] . . . VII
A.8 Total pressure ratio over the first stator row from the E^3 LPT performance report [1] . . . VIII

List of Tables

3.1 2D physics model 17
3.2 Model parameters 17
3.3 Chemistry coupling 23
3.4 Chemistry parameters 23

4.1 First set of values for GCI 27
4.2 Flow result summary 33
4.3 Parametric sweep of TOF for $\%X_{NO}$ 35
4.4 Parametric sweep of TOF for $\%N_{NO}$ with dynamic partial pressures 38
4.5 Parametric sweep of TOF for $\%N_{NO}$ with constant partial pressures 39

1
Introduction

1.1 Background

Nitrogen oxides (NO_X) are some of the most damaging of aircraft emissions and finding methods for reducing them is a priority for the industry as a whole and will be the focus of this investigation. While most NO_X emissions occur at cruise level [3], emissions regulations usually target the Landing and Take-off cycle (LTO).Hence, NO_X emission reduction is important for all phases of the flight and important targets for further investigation .

NO_X, x={1,2} leads to the increased effects of global warming by acting as an indirect greenhouse gas due to the creation of background O_3 as per ICAO [3], through reactions with UV light and atmospheric gases. It also reduces the local air quality around airports contributing to the creation of smog and directly impacts human health as it can cause severe respiratory diseases and premature death. Due to this, regulations on NO_X emissions have, for a long time, greatly impacted the design and development of aircraft engines.

Higher efficiency in turbofans could be achieved with higher overall pressure ratios (OPR), but it is precisely lower OPRs that reduce NO_X emissions [4]. A system or process which reduces NO_X at a turbofan exhaust equivalent to catalytic converters that exist today would give the aerospace industry the possibility of fully exploring new highly efficient designs and, as such, not only reduce NO_X, but also lead to new developments that have second order effects on fuel consumption and all other emissions and this distinct possibility is the main motivator for the pursuit of this thesis.

1.2 Turbofans

Turbofans are the type of jet engine most commonly used in commercial aviation and most recently in military aviation due to its extreme fuel efficiency.
Just like in a turbojet, a fan sucks in freestream air and compressors increase the pressure of the flow in the core before being ignited in the combustor together with aviation fuel. This high temperature jet then powers the turbines, which in turn power the compressors and fan.

The main difference, in a turbofan, is that a portion of the air at the fan outlet bypasses the core and rejoins the flow at the exhaust nozzle. This part of the

flow is being worked on by only the fan like in a propeller engine and thrust is produced at the nozzle by both the core flow and bypass flow. The bypass greatly reduces noise, SFC (improves fuel efficiency) and emissions while also achieving greater thrust at lower speed.

1.3 NOx

Nitrogen dioxide and Nitrogen monoxide, NO_2 and NO respectively, are the species generally referred to as NOx. NO is mostly formed in the combustor with some slower formation happening post-combustion promoted by the high temperatures in the flow. The overall reaction (without reaction steps) is:

$$N_2 + O_2 \rightleftharpoons 2NO \tag{1.1}$$

This reaction is also highly temperature sensitive which is why a small change in temperatures in the combustor can greatly increase resulting NO concentration. As the exhaust cools some NO will oxidize, forming NO_2 through a variety of pathways.[5]

1.4 Catalyst

A catalyst is a compound that induces reactions by lowering the reaction barrier. Catalysis is the process of speeding up the rate of chemical reactions by, for example, lowering the temperature needed to start it without the catalytic agent itself being consumed in the process. Catalysts, in other words, lower the activation energy required for the desired chemical reaction to occur. This results in the catalyst making it easier for chemical bonds to break up and form new substances which will, in the case of this project, be less harmful [6].

In the transport sector, catalysts are present on almost all internal combustion engines that use gasoline or diesel as fuel in the form of a catalytic converter. They are most commonly placed in the exhaust system right after the engine and before the gas mixture is released back into the atmosphere. The gas mixture is forced through a honeycomb structure coated with the catalyst to affect as much of the gas as possible. This type of configuration maximizes the surface area for catalysis and slows the flow, maximizing the reaction rate. However, a honeycomb would disrupt the flow inside a turbofan engine core, directly impacting its overall efficiency and ability to generate thrust.

A turbofan is also an extremely harsh environment with temperatures in excess of $1600K$ at the combustor exit and transonic flow effects ($M_{ax} > 0.5$) making traditional catalytic converters prone to degradation.

This is why the mechanism for catalysis that was selected for study in this thesis is a novel highly durable alloy that coats the stator vanes and non rotating parts

of the hub and the casing of the low pressure turbine (at the LPT the flow has cooled significantly and conditions are such that degradation should be minimal).

A Ni-Co-Pt alloy was selected and modeled in previous work for its high-temperature performance with performance metrics obtained from DFT simulations.

The main reaction with the catalyst for reducing NO_X concentration will be the coupled NO reduction and CO oxidation reaction which can, ignoring the intermediate steps, be understood as:

$$NO_{(g)} + CO_{(g)} \rightarrow \frac{1}{2}N_{2(g)} + CO_{2(g)} \tag{1.2}$$

It should be noted that, in the intermediate steps, some intermediates are adsorbed into the surface and, at the end all of them are desorbed back into the flow with the end result being that the mass balances in the surface and flow do not change with the reactions.

1.5 Main Goals

This thesis aims to analyze the possibility of implementing a catalyst in the LPT of turbofan engines through the use of CFD. The overall goal is to estimate the degree (ratio) of NO_X that can be reduced from the exhaust gases upon introduction of the catalysis mechanism. The overall workflow was as follows:

- From existing geometry provided by NASA from the E^3 project, create a simple 2D RANS $k-\epsilon$ model of the LPT first stage stator row paired with their provided flow inlet data.
  - Refine points of interest in the mesh (boundary layers, stator wakes etc.).
  - Rerun simulations to match inlet and outlet values with provided data.
- Move up to a $k-\omega$ model to better capture the flow and continue refining.
  - Experiment with methods to be used for the refinement of the LES mesh.
  - Couple simulations to catalyst surface chemistry on the stators, and possibly other surfaces, in the simulation (provided by a parallel thesis as well as by the thesis supervisors).
  - Validate flow results of the simulations through GCI
- The ultimate goal of running RANS and LES 3D simulations, with and without chemical reactions, was not achieved due to time limitations but it was still a focus to lay groundwork for this future work which will consist of:
  - Run 3D RANS simulations of the first stage.
  - Refine mesh in preparation for LES simulations.
  - Run 3D LES simulations.
  - Validate the results of the simulations through GCI.
  - Scale results to predict the catalyst's overall impact on NO_X concentration at LPT outlet.

1.6 Limitations

In this section, the scope and limitations for the thesis will be defined in more detail.

This thesis is only intended to look at the Low Pressure Turbine. Other elements of the engine such as the High Pressure Turbine (HPT), the Combustor, the High Pressure Compressor (HPC) and the Low Pressure Compressor (LPC) are not part of the scope for this thesis and thus will have limited mentions.

In the five stage LPT of the E^3 engine, the focus was on the first stage, to limit the scope. Only one row of stators will be included and simulated. Timetable permitting, a second stator row could have been added to further boost the catalyst surface area. However, the flow is not affected by the chemistry but the chemistry is highly sensitive to the flow conditions. As the reaction rates were shown to be almost directly proportional to local pressure and velocity conditions [7], it should be feasible to scale results for more stages and this was seen as an adequate demarcation.

The main goal of this thesis was to evaluate the net reduction in NO_X due to the catalyst and, as such, depends on modeling the chemical reactions on the surfaces of the stators of the LPT. The chemical reactions of the catalytic agent will be implemented in terms of surface chemistry and fluxes on surfaces that have the catalytic coating applied. The chemistry model was adapted from the parallel thesis [7] in consultation with the supervisors.

Thorough durability and degradation analysis of catalyst coating materials was also not performed. Catalyst placement at LPT inlet is assumed to be sufficiently far away from potentially degrading conditions such as those in the HPT. Although the novel catalyst studied here was designed for high durability, a study on the effects of surface roughness could have been performed if not for time limitations (surface roughness has the potential to greatly increase rates of reaction with NO_X but would have significant effects on turbine performance).

1.7 Ecological and Environmental Objectives

As mentioned in Section 1.1 NO_X emissions have a significant impact on the environment and human health but could be significantly reduced by the novel catalytic conversion method evaluated in this thesis. The goal of this thesis was to provide a proof of principle that could motivate experimental work in the area. If successful, this coud bring about great changes in the aviation industry and great benefits to the environment and humanity at large.

As mentioned previously, NO_X regulations also significantly limit turbofan design with more efficient engine designs being feasible but sometimes avoided due to their NO_X emissions. For most modern turbofans, it can be assumed that the

reduction of NO_X emissions in the design phase generally leads to an increase in SFC (Specific Fuel Consumption) [4]. It is then the case that a reduction of NO_X emissions through use of this novel catalytic coating could lead to more efficient engine designs (with lower SFCs) while still complying with current limits to NO_X emissions.

2
Theory

2.1 Turbulence

Turbulence, mainly due to the work of Richardson and Kolmogorov starting in 1941, is classically understood as an energy cascade through progressively smaller vortices (hereafter referred to as eddies). The larger eddies are formed from the turbulent kinetic energy (known as TKE or k) in the flow, so they are non-universal, i.e. their characteristics depend on the flow. The rest of the eddies are universal and can be divided into; the energy transfer region, where energy is transferred into progressively smaller eddies but viscous effects are still negligible; and the destruction or dissipation region, where viscosity dominates and the smallest possible eddies are transformed into heat and destroyed. Figure 2.1 is a graphical representation of these length scales on a log plot of eddy energy for different wave number values (Wave number $= 2\pi/$Eddy diameter

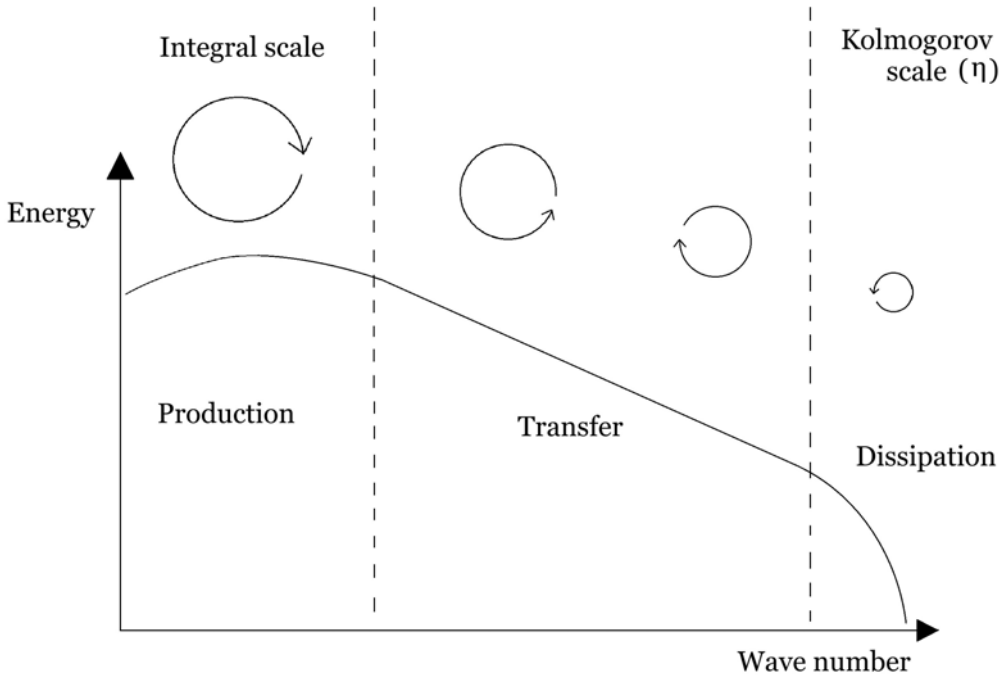

Figure 2.1: The different length scales in a turbulent energy cascade

Kolmogorov assumed the smallest eddies to be dependent on viscosity, ν (m^2/s), and turbulence dissipation rate, ϵ (m^2/s^3). Through dimensional analysis, the scale of these Kolmogorov microscale eddies can be estimated to be (this scale being denoted by η):

$$\eta(\mathrm{m}) = f\left(\epsilon(\mathrm{m}^2/\mathrm{s}^3), \nu(\mathrm{m}^2/\mathrm{s})\right) \qquad \Rightarrow \qquad L^1T^0 = (L^2T^{-3})^m(L^2T^{-1})^n \Rightarrow$$

$$\Rightarrow \begin{cases} 1 = 2m + 2n \\ 0 = -3m - n \end{cases} \Leftrightarrow \begin{cases} m = -\frac{1}{4} \\ n = \frac{3}{4} \end{cases} \Rightarrow$$

$$\eta = \left(\frac{\nu^3}{\epsilon}\right)^{\frac{1}{4}} \tag{2.1}$$

Similarly, for larger eddies (known as integral eddies), it is known that production dominates and so it can be assumed they depend on TKE, k (m^2/s^2), and dissipation rate, ϵ (m^2/s^3). The scale of these eddies can be called l_0, and estimated using dimensional analysis:

$$l_0(\mathrm{m}) = f\left(k(\mathrm{m}^2/\mathrm{s}^2), \epsilon(\mathrm{m}^2/\mathrm{s}^3)\right) \qquad \Rightarrow \qquad L^1T^0 = (L^2T^{-2})^m(L^2T^{-3})^n \Rightarrow$$

$$\Rightarrow \begin{cases} 1 = 2m + 2n \\ 0 = -2m - 3n \end{cases} \Leftrightarrow \begin{cases} m = \frac{3}{2} \\ n = -1 \end{cases} \Rightarrow$$

$$l_0 = \frac{k^{\frac{3}{2}}}{\epsilon} \tag{2.2}$$

This result proves highly useful for mesh evaluation and is used further in section 3.5.

2.2 CFD

Computational Fluid Dynamics (CFD) is a popular tool used to simulate and analyze complex flow problems using numerical analysis. CFD simulations are fundamentally built upon the Naiver-Stokes equations as well as the three conservation equations. They are described in more detail in Section 2.2.1.

CFD programmes perform the necessary calculations so that they can simulate the flow of a specified fluid and how it interacts with regions and surfaces that have been defined by boundary conditions. The results of these simulations can later be compared to those from experimental tests involving test rigs set up with the same initial and reference conditions.

2.2.1 Navier-Stokes Equations

The Navier-Stokes equations in short are Partial Differential Equations (PDEs) that are used to describe motion and how momentum changes in viscous fluid substances due to applied forces [8]. The governing equations central to a fluid, being the three aforementioned conservation equations are briefly described and written on differential form below:

Conservation of mass equation states that mass cannot be created or destroyed in a control volume and thus, the difference in mass flow between the inlet and outlet is equal to zero.

$$\frac{\partial \rho}{\partial t} + \nabla \cdot (\rho v) = 0 \tag{2.3}$$

The conservation of momentum equation, sometimes also referred to as the Navier-Stokes equation. It implies that, in a control volume, the momentum is neither created or destroyed and can only change through forces applied on the fluid in accordance with Newton's Second Law of Motion $F = M \cdot a$.

$$\frac{\partial}{\partial t}(\rho v) + \nabla \cdot (\rho v v) = -\nabla p + \nabla \tau + \rho g \tag{2.4}$$

The conservation of energy equation is the first law of thermodynamics. It states that the total sum of work done and heat added to the system will increase the total energy of said system.

$$\rho \left[\frac{\partial h}{\partial t} + \nabla (h \cdot v \right] = -\frac{\partial p}{\partial t} + \nabla (k \nabla T) \cdot \phi \tag{2.5}$$

2.3 RANS

Reynolds-averaged Navier-Stokes (RANS) is one of the most used numerical methods when it comes to simulating fluid dynamics problems. It uses time-averaged equations of motion in the flow to primarily describe the flows turbulence. Said equations use approximations of the properties in a turbulent flow to provide approximate time-averaged answers to the governing Navier-Stokes equations. It is one of the most computationally inexpensive tools to use in CFD because it does not resolve the flow exactly but provides models of approximate, time-averaged solutions.

2.3.1 RANS EVM

Reynolds Averaged Navier-Stokes Eddy viscosity Model is a commonly used CFD approach when modeling turbulent flows by assuming the turbulence is a purely diffusive process and the Reynolds stress tensor is related to the eddy viscosity (μ_T). The equation RANS EVM is based on is called the Boussinesq approximation and it looks like this:

$$\rho(\overline{u' \cdot u'}) - \frac{2}{3}\rho k = -\mu_T(\nabla U + (\nabla U)^T) \tag{2.6}$$

Where μ_T is the aforementioned eddy viscosity, k represent the turbulent kinetic energy, U is the averaged velocity field and $u\dot{t}$ represents velocity fluctuations.

2.3.2 $K-\epsilon$

The most widely used two-equation eddy-viscosity models today is called the $K-\epsilon$ turbulence model. The model is essentially attempting to predict turbulence during the simulation by solving for the turbulent kinetic energy (k) and the turbulent dissipation rate (ϵ) through two different partial differential equations. It is a very robust model that works well for freestream flows. It does however struggle to model turbulence near walls where fluids slow down and k effectively drops to zero. To counteract this, $K-\epsilon$ models require viscous damping functions that limit the behavior of k and ϵ at walls.[9]

$$k \approx y^2 \text{ and } \frac{\epsilon}{k} \approx \frac{2\nu}{y^2} \text{ for } y \to 0 \tag{2.7}$$

Here, y represents distance from the wall.

2.3.3 $K-\omega$

Another commonly used two-equation eddy-viscosity model is the $k-\omega$ turbulence model. The workflow for this model is similar to that of $k-\epsilon$ except it attempts to solve for specific dissipation rate (ω) instead of turbulent dissipation rate (ϵ). ω measures dissipation per unit turbulent kinetic energy (ϵ/k) with some referring to it as a frequency [10]. It behaves better than ϵ near walls and is more accurate. It does, however, require a very fine boundary layer mesh with a $Y+ \leq 1$.

2.4 LES

Large eddy simulation (LES) is a model in CFD used for a wide array of engineering problems that involves solving complex turbulent flows. It numerically solves Navier-Stokes equations by resolving large flow scales and modeling the small flow scales. These flow scales is what is often referred to as "eddies" when using LES. The user determines how many of these eddies will be resolved and modeled respectively by setting up a filter size of their own choice. All eddies larger than this filter size will be resolved, meaning directly computed solutions. Meanwhile, all eddies smaller than the filter size will be modeled, meaning approximated solutions.

This simulation model serves as a compromise between RANS that models (approximates) the entire flow and Direct Numerical Simulation (DNS) which resolves/numerically solves the entirety of the flow. DNS is the most accurate simulation model since it directly computes the Naiver-Stokes equations for the entire flow. Because of this, it is also the most computationally expensive one, making it impractical for simulations involving complex geometries and large flow configurations.

2.5 Chemistry for Catalytic NOx Reduction

As previously mentioned, equation 1.2 is the main reaction to be looked on for reducing NO_X concentrations in the flow. It highlights how NO can be reduced by residual CO that remains in the exhaust gas due to incomplete combustion. CO simultaneously oxidizes and the net result is the conversion into gases with lesser environmental impact, namely N_2 and CO_2.

2.5.1 Microkinetic Model

Microkinetic modeling is a useful tool in chemical engineering that can help with streamlining the whole process of catalyst designing. They provide information regarding reaction intermediates and the rate-determining step for elementary reactions, information that is vital when trying to design an improved catalyst [11]. A microkinetic model is considered a 0D simulation since it has no set geometry, no spatial coordinates and focuses purely on reactions at the molecular scale over time at a given reaction site. Each reaction step of the reaction network leading to an intermediate or product is assigned a rate expression as function of the reaction constant and concentration of reacting species. Together the reaction network forms an equation system and its solution determines the speed of the overall chemical reaction. It ultimately helps to calculate the rate of reaction for all species present under the set operating conditions.

2.5.2 Active Site Density & Turnover Frequency

One of the most important metrics for measuring activity in a catalyst is called the turnover frequency and it is "the number of chemical conversions of reactant molecules per catalytic site and per unit time" [12] or, effectively, the overall catalytic reaction rate divided by the active site density. With the turnover frequency being a metric for activity, a higher TOF value is indicative of a better catalyst.

The total number of catalytic locations is called the active site density. It can be measured either across a surface area or in a volume [12], however, for the sake of this thesis it is strictly over the surface area of the stators, along with the hub and casing in the stator section of the LPT.

$$TOF = \frac{\text{Overall Reaction Rate}}{\text{Active Site Density}} \tag{2.8}$$

2.5.3 Species Transportation

All relevant chemical species in a system like NO, CO and such travel through the domain in a diluted solution. Meaning that they, on a global scale make up for a small percentage of the total concentration at any given location. A particular physics model in COMSOL named "Transport of Diluted Species" can be used to simulate diffusion, transportation and convection of the diluted species in the fluid bulk throughout the computational domain [13]. Transport of the reactive species to the active site can thus be as important as the intrinsic reaction rate of the site when determining the overall reaction rate.

3

Methods

3.1 2D Geometry

Geometry for the Low Pressure Turbine (LPT) was supplied by NASA. In order to facilitate the collection of data needed to set initial conditions and validate the CFD, the same geometry used in the NASA Energy Efficient Engine (E^3) programme in the 1970s was used in this thesis. The geometries for the respective rotors and stators, as well as the complete assembly, were provided in the form of CAD .igs files. From these files, the stator pitch-line profile in Figure 3.1 of the blade was extracted, rotated to be aligned with the xy axis while preserving their z-axis angle and flattened with minimum deformation in the CAD software Rhino (the entirety of the pitch-line was not fully in the same plane). These profiles were then used to run the 2D simulations while the entire blades will be used in the 3D simulations.

The E^3s Flight Propulsion Systems (FPS) LPT has a total of five, highly loaded stages [2]. However, this project will focus on just four gaps from within the first stage stator row for 2D simulations. The spacing for said gaps was approximated from the mid radius perimeter as follows:

$$S \approx \frac{2\pi r_{mid,S1}}{n_{S1}} \Rightarrow S \approx 0.032995\text{m}$$

With $n_{S1} = 72$ being the number of stators in the first stage [1] and $r_{mid,S1} = 0.3781$m being an approximate radius (from the engine centerline) for the points of the stator pitch-line.

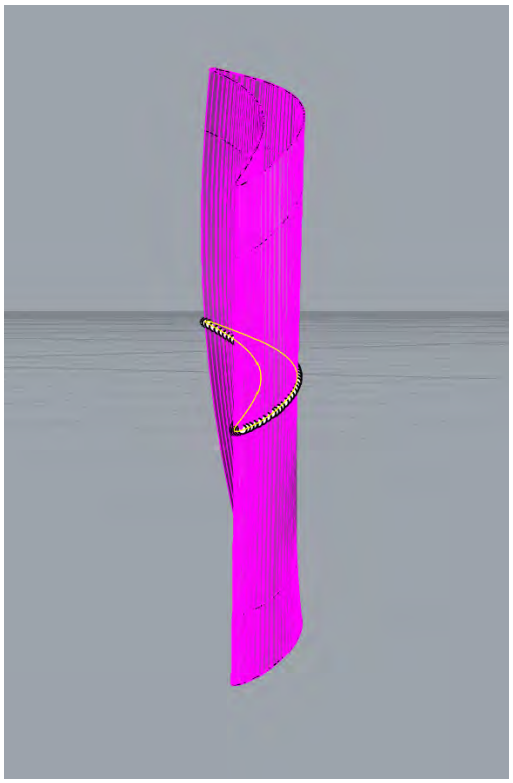

Figure 3.1: Pitch-line highlighted in original NASA first stator geometry

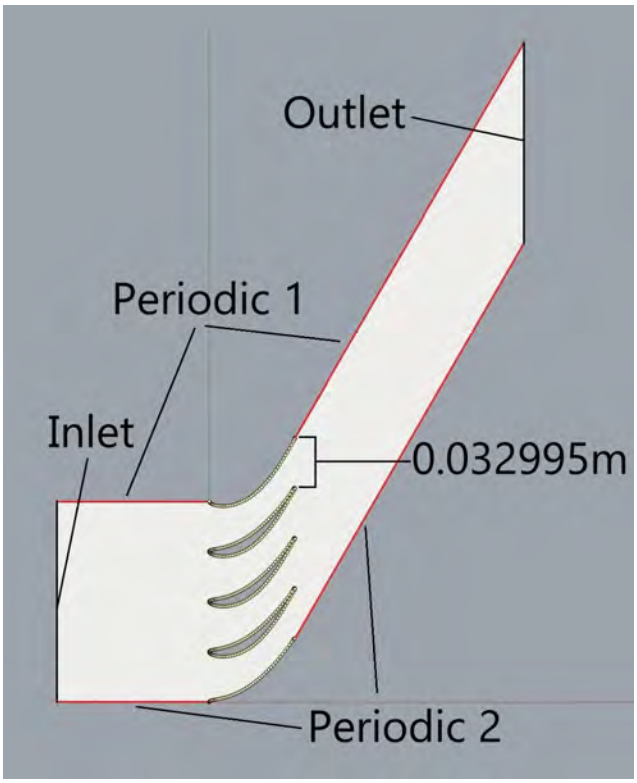

Figure 3.2: Flattened Pitch-lines arrayed in finalized 2D geometry

The origin is aligned with the bottom half stator leading edge and 5 stator vanes and 4 gaps are modeled. At the arrayed stator vane walls (including the top and bottom half stators), a no-slip condition was set. As seen in Figure 3.2, the top and bottom walls were set with a periodic condition. Even though the periodic condition makes this unnecessary from a simulation point of view, the outlet side periodic walls were angled at a rough approximation of the stator exit angle.

This exit angle will not perfectly match the simulated one but helps with visualization and in early trial runs allowed for a slip condition instead of a periodic one for easy meshing and computations.

3.2 Meshing and Numerical Setup - 2D RANS

For the first simulations, velocity at LPT inlet came in with zero degrees swirl with data on inlet and outlet conditions taken from [1]. An incompressible $k-\epsilon$ turbulence model was used for first runs and then replaced with a $k-\omega$ model for better handling of the flow. COMSOL uses a triangular mesher for the domain, periodic boundaries, inlet, and outlet and a prismatic mesh was used for the no-slip boundaries.
This initial mesh is shown in Figure 3.3 and the bottom half-stator to periodic boundary transition can be seen in more detail in Figure 3.5. Figure 3.4 shows the leading edge boundary layer mesh of one of the full stator vanes in the domain.

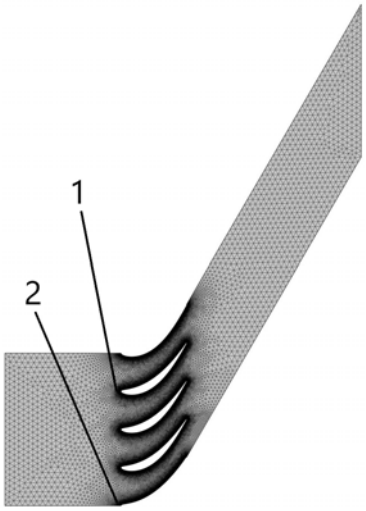

Figure 3.3: Initial 2D mesh

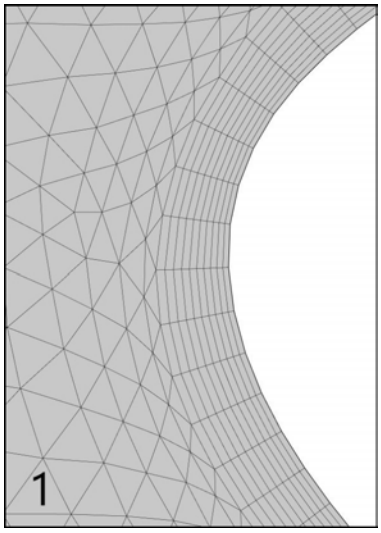

Figure 3.4: Detail 1

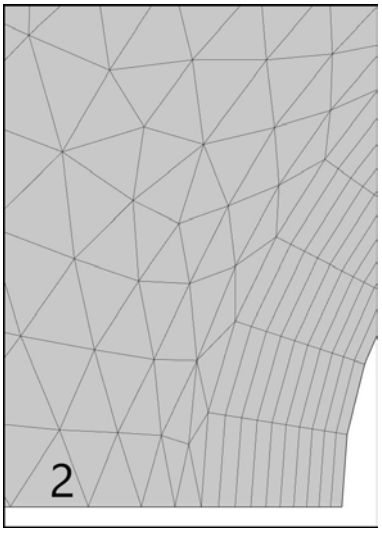

Figure 3.5: Detail 2

From these runs, the real exit flow angle was obtained and used for mesh control edges for wake refinement for the following runs.

Distribution nodes were added along these exit flow angles and along the periodic boundaries towards the outlet, resulting in the mesh seen in Figure 3.6 with a total cell count of 232780.

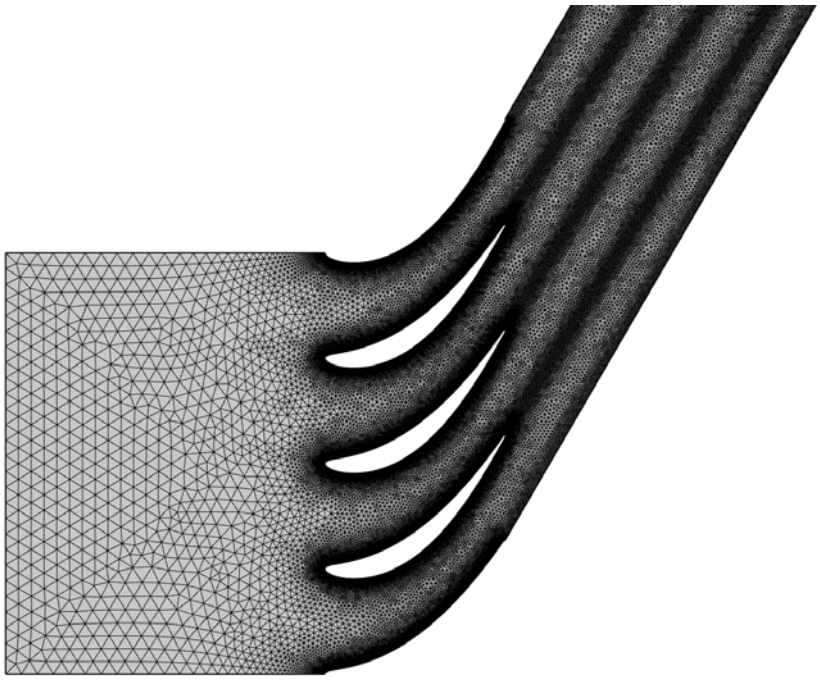

Figure 3.6: Added detail along exit flow angles

3.2.1 Mesh Refinement

In order to eventually move up to a $k - \omega$ model the mesh needed to be even more refined to properly simulate the flow behavior, especially when it comes to resolving the boundary layers on the stators. For this, a $Y+$ calculation was made to determine an estimated thickness for the first boundary layer with a target value of $Y+ \leq 1$. This equated to a thickness of $2.2 \cdot 10^{-6}$ m for the first boundary layer. To smoothen the transition from the boundary layers to the freestream mesh and eliminate element skewness, a total of 35 layers was used with a growth factor of 5% that can be seen in Figure 3.7.

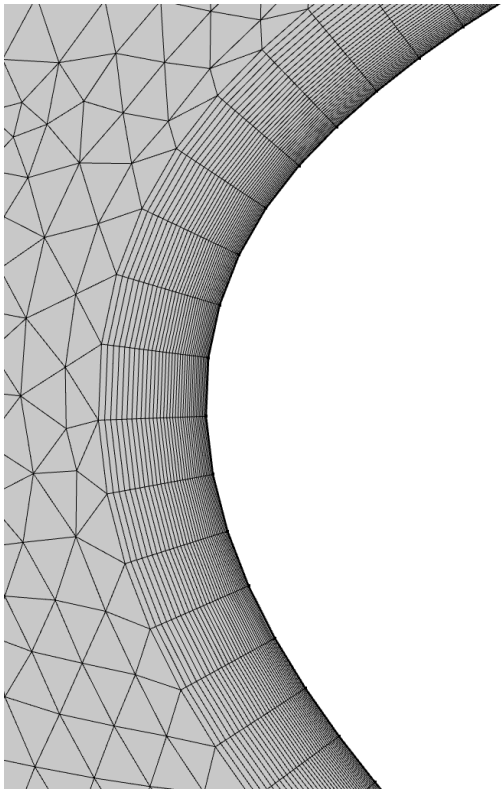

Figure 3.7: Refined Boundary slayers

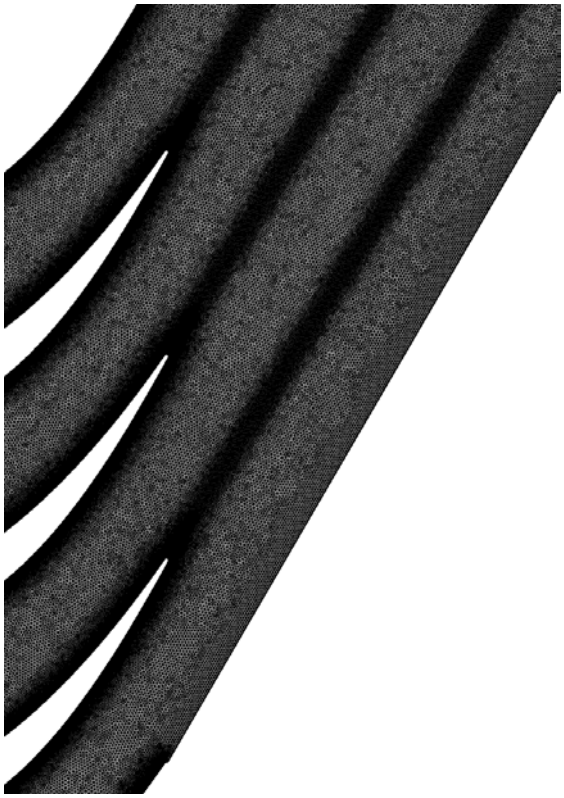

Figure 3.8: Further wake region refinement

The mesh quality in the freestream, particularly the wake region was further refined as seen in Figure 3.8, in order to capture realistic flow behavior behind the stators. This was done by decreasing the overall element size parameters for the freestream mesh as well as lowering the maximum element growth rate. The total cell count for the refined 2D mesh ended up being 765717.

3.2.2 Numerical Setup

To be able to actually use the refined mesh in COMSOL, a first simulation needed to be run with the $k - \omega$ model on the coarser mesh from Figure 3.6. The results of this run was then imported as initial values to the simulation with the refined mesh.

The inlet conditions for the $k-\omega$ model were updated to match HPT outlet data in Appendix A.4 from high fidelity simulations (see Table 3.2). Velocity, temperature and pressure at 50% of blade height was used as a good approximation of the pitchline conditions. Inlet Mach was calculated from the other given inlet conditions. Outlet static pressure was obtained through a total-to-static pressure ratio over the stators ($P_{T,inlet}/P_{S,outlet}$) of 1.28 from Table XIII in the test vehicle performance report [1]. The ratio of specific heats (γ) was assumed to be 1.33.

Table 3.1: 2D physics model

Turbulent flow
High Mach Number flow
Compressible flow
$k-\omega$
Wall treatment
Stationary
No slip walls on stators
Periodic condition boundaries

Table 3.2: Model parameters

Parameter	Value	Unit
Inlet velocity	176.97	m/s
Inlet total temperature	1117.89	K
Inlet total pressure	829720	Pa
Inlet Mach	0.273	1
Outlet static pressure	648218	Pa
γ	1.33	1

Table 3.1 shows the setup of the physics model used for the final simulations. The turbulence model was also updated to a compressible high Mach number flow model for more realistic modelling of higher Mach sections of the flow. All surfaces where boundary layers are present were set up with no slip walls and all boundaries normal to the flow were set to periodic condition. Total temperature, total pressure and Mach number was set at the inlet while only static pressure was set at the outlet. The wall treatment in the physics model was set to automatic. This means it will use a low Reynolds number method near all solid walls where the boundary layer mesh is fine enough (i.e. where $Y+ \leq 1$) and use wall functions near walls where the mesh is too coarse ($Y+ > 1$).

3.3 3D Geometry

A similar approach was used for the 3D geometry, although, due to the annular geometry of an axial turbine, the periodicity will be rotational instead of translational as it was in the 2D approximation. Since only stators and no rotors would be simulated a single stator vane is included to make computations less cost-prohibitive. To this effect a $1/72$ slice was extracted from the LPT hub, casing, and stator row, ignoring subsequent rotor row and stages. An illustration of this slice can be seen in Figure 3.9 below:

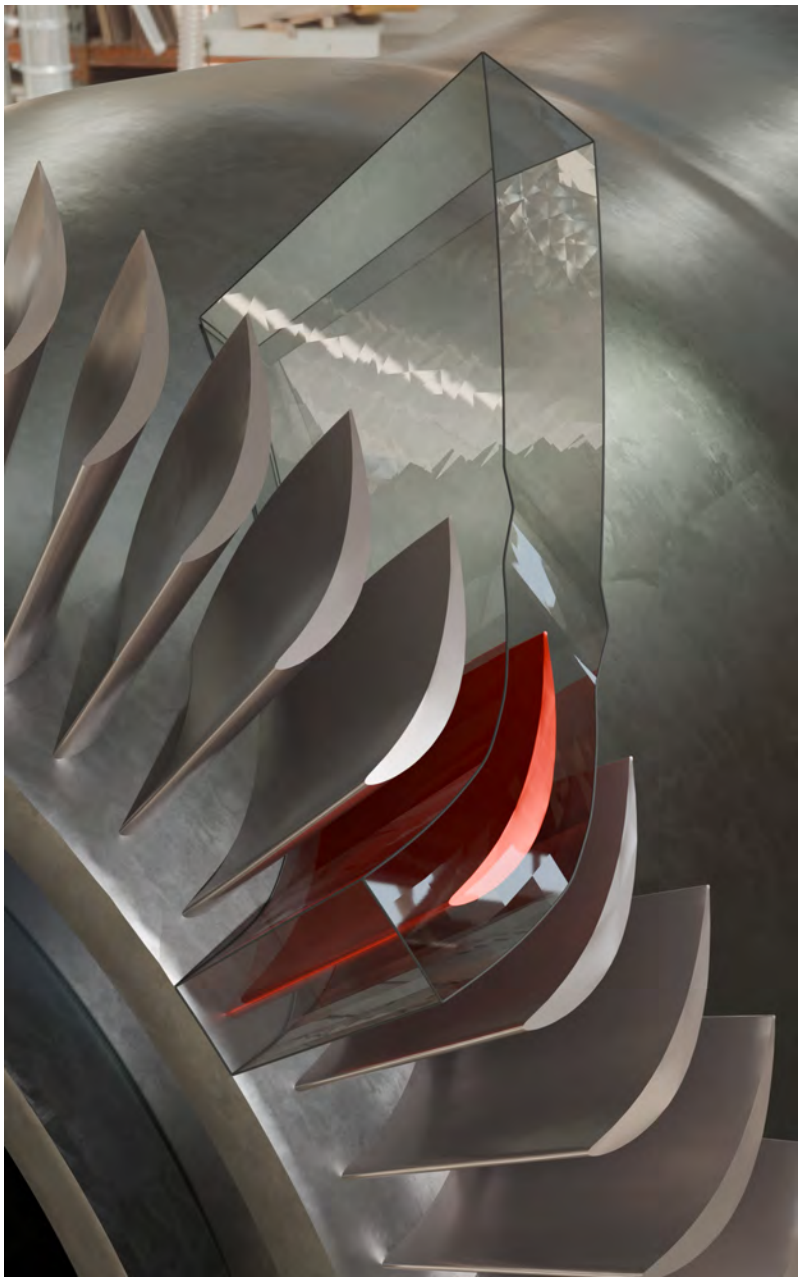

Figure 3.9: Highlighted domain that was simulated in 3D with the vane that was included in red

The side walls have a periodic condition and the inlet and outlet are normal to the axial direction to allow for the periodic walls to be exact copies of each other rotated by $1/72$ of a full rotation. The upper and lower surfaces have a no slip condition since, in 3D, these are a slice of the casing and hub respectively. The stator surfaces are also set to no-slip just like in 2D. The entire 3D geometry was modelled in blender from the original .igs files provided by NASA and converted to a .STEP format in Fusion 360, and finally composited in COMSOL.

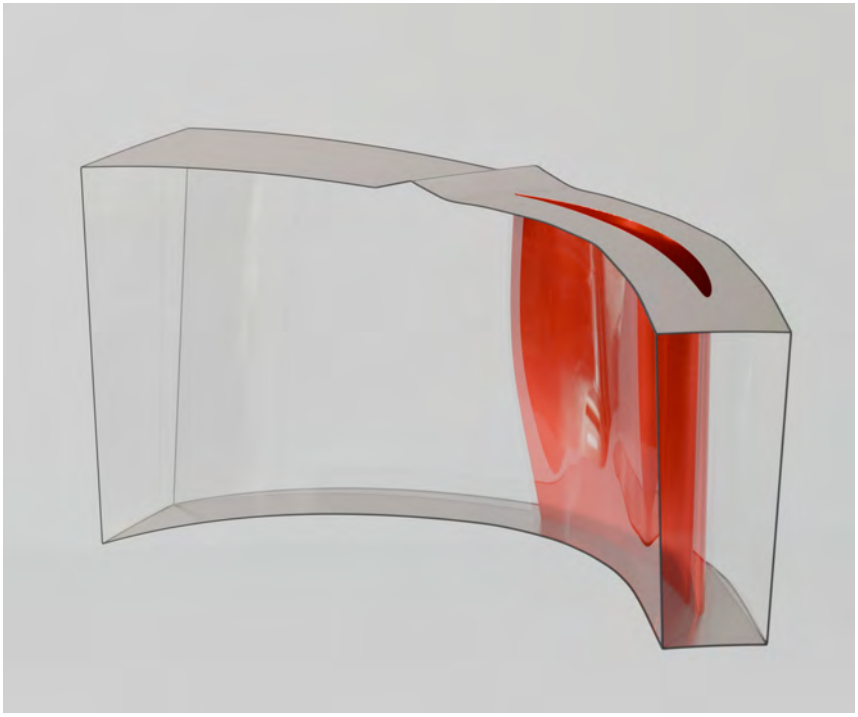

Figure 3.10: Final 3D geometry with hub and casing in gray, stator in red, and glass representing the fluid domain

3.4 Meshing and Numerical Setup - 3D RANS

3.4.1 Meshing

As mentioned previously, in 2D, the same "distribution" was applied on periodic faces, ensuring the same cell face size and location on periodic boundaries. For 3D simulations this is not enough, as the cell faces are now 2D faces instead of line segments. To possibilitate periodicity on the side walls, an "identical mesh" condition had to be used which significantly hindered meshing (more on this in Section 4.7). For 3D Boundary layers are set up on all the physical walls in the fluid domain, i.e. the stator as well as along the hub and the casing. Unlike in 2D, for 3D only one mesh is generated. The maximum and minimum element sizes of mesh cells are much smaller around the stator compared to the freestream.

Because of issues that arose with the identical mesh function, the highest quality mesh that was successfully computed for this thesis contained 5 Boundary Layers on the stator, hub and casing. The total cell count was 4670679. This mesh took around three and a half hour to generate, more details on this process is in Subsection 4.7.1.

3.4.2 Numerical Setup

3D inlet conditions were also taken from the HPT outlet data seen in Appendix A.4 that was mentioned previously. The available data only has conditions at 28

points going from 6.667% to 96.667% of inlet height instead of a continuous field so the rest had to be interpolated. The radial location of these data points were given in percentage. Thus, they were converted to mm by multiplying with 81.128mm (the height of the LPT inlet). The Azimuthal velocity from this data was unusual. Seeing as old E^3 design papers indicate that the LPT inlet to be designed for zero degrees inlet swirl, it was agreed with the NASA team that assuming the azimuthal swirl to be zero degrees for all points was an appropriate assumption.

3.5 Mesh Refinement for LES

In order to perform LES, mesh refinement is required. The LES simulation, needs a mesh refined enough to resolve 80% of eddies. Hence, the eddies present in a certain region has to be bigger than the cell size in said region. The sketch bellow attempts to make this idea clearer.

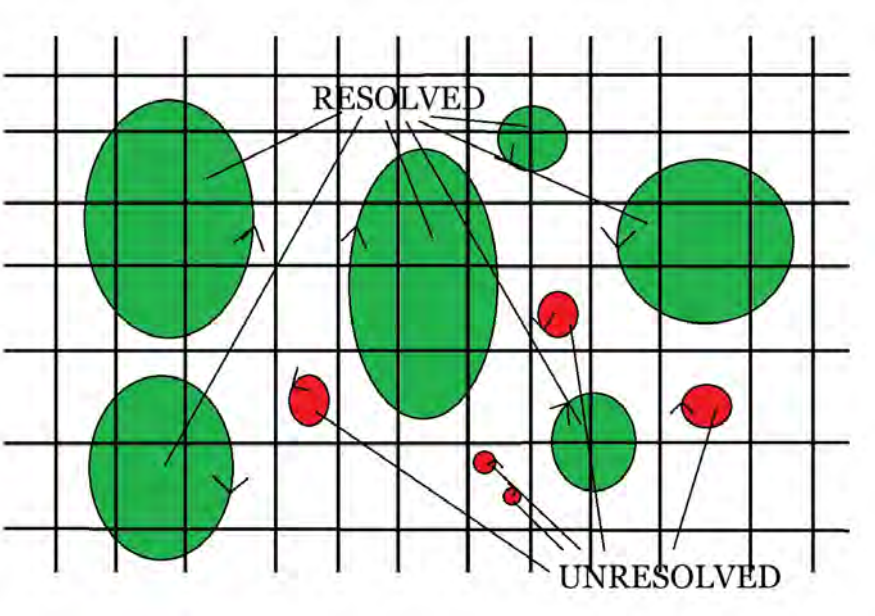

Figure 3.11: Example of size of eddies vs mesh size required to resolve them

To allow the mesh to perform this way, cell length that is one fifth of the local integral length scale is seen as a good approximation.

The integral length scale calculated in section 2.1 is a good tool for knowing the approximate size of eddies in a region. With a highly turbulent region, turbulent kinetic energy is higher and the larger eddies (the ones with no viscous effects) will be larger and all the eddies from the energy cascade will be larger.

In this study, final RANS calculations will be done using the $k-\omega$ turbulence model and it is known that ω can be obtained from ϵ:

$$\omega = \frac{\epsilon}{C_\mu k} \tag{3.1}$$

With $C_\mu = 0.09$ being an empirical coefficient.
From equations 2.2 and 3.1, the integral length scale can be rewritten for the $k-\omega$ turbulence model as follows:

$$l_0 = \frac{\sqrt{k}}{C_\mu \omega} \tag{3.2}$$

In order to put into use the previous assumption of one-fifth of integral length scale, a plot can be done where the fraction of integral length scale over significant mesh length is evaluated over the whole domain (let us call this fraction $f_{fineness}$):

$$f_{fineness} = \frac{l_0}{\Delta} \qquad \text{with} \qquad \Delta = \text{local mesh cell volume}^{1/3} \tag{3.3}$$

And, in this plot, it will be clear which areas of the mesh will need refinement before LES can be performed ($f_{fineness} < 5$), and which areas already have a fine enough mesh ($f_{fineness} > 5$).

3.6 Numerical Setup - LES

Instead of the traditional Smagorinsky model for subgrid-scale modelling, the plan for the LES simulations in this thesis is to use the WALE model (Wall-Adapting Local Eddy-viscosity) first detailed by F. Nicoud and F. Duros [14]

Compared to the Smagorinsky model, WALE offers a few key advantages:

- Rotation and local strain now both affect eddy viscosity instead of being dependent only on local strain rate and the subgrid characteristic length scale.
- Damping functions are not necessary as in traditional LES since eddy viscosity now naturally goes to zero at walls.
- More realistic turbulent to laminar transition since eddy viscosity goes to zero when there is pure shear.

3.7 Chemistry Implementation

The chemistry interface that is used in this thesis was built in collaboration with a chemical engineer running a parallel thesis on the same subject with a greater focus on the chemistry[7]. Partial pressures for the different chemical species were calculated using species mole fractions (xNO, xCO etc.) obtained from J. Moder, NASA Glenn Research Center through personal communications A.4. These are in turn dependent on the pressure. A nickel (Ni), cobalt (Co) and platinum (Pt)

combination is shown to be a promising catalyst candidate in a computational screening study [15]. In the alloys, cobalt is used to give thermal stabilization while platinum acts as the catalytically active component for the NOx conversion. The planar density of an ideal FCC(100) nickel face divided by Avogadro's constant ($N_A = 6.022 \cdot 10^{23}$mol^{-1}) gives the ideal molar site density for a smooth catalysts surface, defined as Γ and measured in units mol/m^2. A reference value for TOF was acquired from [15] at a temperature of 1100K, close to operating temperatures for the LPT. This reference TOF was then scaled up to to the correct operating pressures of the LPT based on the previously mentioned partial pressures. This was in turn adjusted to an effective TOF to account for differences in local inlet concentrations based on partial pressures calculated from data in Appendix A.4. Local inlet concentrations are denoted as cNO$_{in}$, cCO$_{in}$ etc.

A 0D microkinetic model was built in COMSOL using a reaction engineering interface together with the main equation 1.2, Γ and effective TOF. The 0D model was simulated in two steps, a stationary plug flow step and a time dependent step. Once done, this model was used to import chemistry (chem), reacting flow and transport of diluted species (tds) interfaces to 2D. Chemistry is a similar interface to reaction engineering, except now it has been assigned to a physical domain. Reacting flow connects two interfaces and ensures that they communicate with each other, in this case the high Mach number flow $k - \omega$ and the transport of diluted species. Henceforth, the chemistry, reacting flow and tds are referred to as the chemistry coupling.

For the chemistry coupling, the walls that were periodic in the flow simulation remained periodic for the chemistry simulation. Stators were assigned flux boundaries using the effective TOF and Γ. At the inlet, previously mentioned inlet values for concentrations were used. Reaction rates for each species are imported into the tds directly from the chemistry interface. Volumetric consumption rate of NO $r_{NO,vol}$ in the diffusion boundary layer was estimated by distributing the Γ and effective TOF over an effective boundary layer thickness (d) obtained from previous work [7].

$$r_{NO,vol} = \frac{\Gamma \cdot TOF_{eff}}{d} \tag{3.4}$$

The settings and inlet parameters for the chemistry coupling of this thesis are about the same as the ones from earlier mentioned previous work [7] with two exceptions. The first one was that the material balance form for the tds had to be changed from nonconservative to conservative in order to account for a much greater density ratio. The second one was to correct a misplaced initial value for the CO concentration.

The idea is that the implementation of the chemistry coupling is the same for both 2D and 3D simulations. The results from resolved stationary flow simulations are imported as "values of variables not solved for" into the time dependent chemistry coupling simulation, using the finest mesh available for both 2D and 3D. The time dependent study length is 0.03s with a step size of 0.005s. Once completed, an

average of NO concentrations (X_{NO}) is taken from both the inlet and outlet in order to plot the % of X_{NO} throughout the simulation like this:

$$\%X_{NO} = \frac{X_{NO,in} - X_{NO,out}}{X_{NO,in}} \tag{3.5}$$

Table 3.3: Chemistry coupling

Chem interface
- Species information
Tds interface
- Flux boundaries on stators
- Reaction rates
- Periodic boundaries
Reacting flow interface
- Connects interfaces

Table 3.4: Chemistry parameters

Parameter	Value	Unit
TOF_{ref}	$3.2 \cdot 10^{-3}$	$1/s$
TOF_{scaled}	$5.2 \cdot 10^{-2}$	$1/s$
TOF_{eff}	varies	$1/s$
Γ	$2.6 \cdot 10^{-5}$	mol/m^2
Inlet concentrations	varies	mol/m^3
$r_{NO,vol}$	$6.6 \cdot 10^{-3}$	$mol/m^3 \cdot s$

3.8 Validation and GCI

Validation is complicated as the data used in the simulations in this study is directly from a specific test rig at specific conditions in order to provide a proof of principle for running further tests with the novel catalytic alloy. Despite test data for the LPT in these conditions not existing, validation is performed with cruise conditions to lend some credence to the results (inlet conditions and results from NASA's performance report [1]).

To eliminate discretization results, the method chosen for this thesis is a GCI (Grid Convergence Index) study.
This method has been shown to reduce and quantify the uncertainty due to discretization and to be adequate for both RANS and LES based CFD simulations [16] [17].

This grid refinement study method has seen ample use but will be briefly described as following (as in [17]):

The study requires at least three simulations for three different grid sizes. Each grid has an average cell length h which is given by:

$$h = \left[\frac{1}{N} \sum_{i=1}^{N} \Delta \forall_i \right]^{1/3} \tag{3.6}$$

Where N is the total number of cells in the domain and $\Delta \forall_i$ is the volume of cell i. For successive grids j and i the grid refinement ratio is then given as:

$$r_{ji} = \frac{h_j}{h_i} \tag{3.7}$$

The difference in solutions for these grids are similarly calculated:

$$\epsilon_{ji} = \phi_j - \phi_i \tag{3.8}$$

Where ϕ is a selected representative solution value (like static pressure ratio). The order of accuracy p is then estimated as follows (example for three grids from coarsest, three, to finest, one):

$$p = \frac{1}{ln\, r_{21}} \left| ln \left| \frac{\epsilon_{32}}{\epsilon_{21}} \right| + q(p) \right| \tag{3.9}$$

$$\text{with} \qquad q = ln \left(\frac{r_{21}^p - s}{r_{32}^p - s} \right) \quad \text{and} \quad s = 1 \times \text{sign} \left(\frac{\epsilon_{32}}{\epsilon_{21}} \right) \tag{3.10}$$

The order of accuracy provides an estimation of how fast the solution converges with grid fineness. From p, GCI can be obtained, which is a widely accepted quantity to report as the numerical error of a CFD simulation and the goal of this mesh refinement study. For three grids the error of the solution for the finest grid, ϕ_1 can be estimated as:

$$GCI_{21} = \frac{1.25 \left| \frac{\epsilon_{21}}{\phi_1} \right|}{(r_{21})^p - 1} \tag{3.11}$$

4

Results & Discussion

4.1 Preliminary 2D Runs

Even though the preliminary 2D runs were not relevant for extraction of flow conditions, it is of some interest to observe the effects of the mesh refinement mentioned in section 3.2. Mainly, the mesh refinement requirements for future 3D LES simulations can be examined, and some of the most important regions can already be identified in these simpler 2D meshes.
By plotting $f_{fineness}$ as calculated in equation 3.3 (with $\Delta =$ local mesh cell volume$^{1/2}$ as this is a 2D case) with a filter for mesh cells with $f_{fineness} < 5$ we get an indicator of the regions that would need a denser mesh for LES, which can be seen in Figure 4.1 and Figure 4.2:

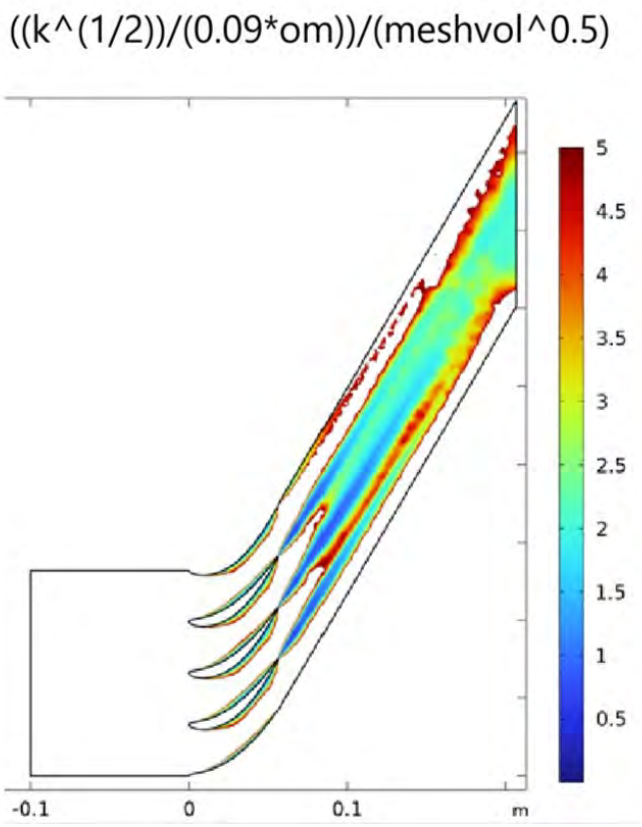

Figure 4.1: Areas with $f_{fineness} < 5$

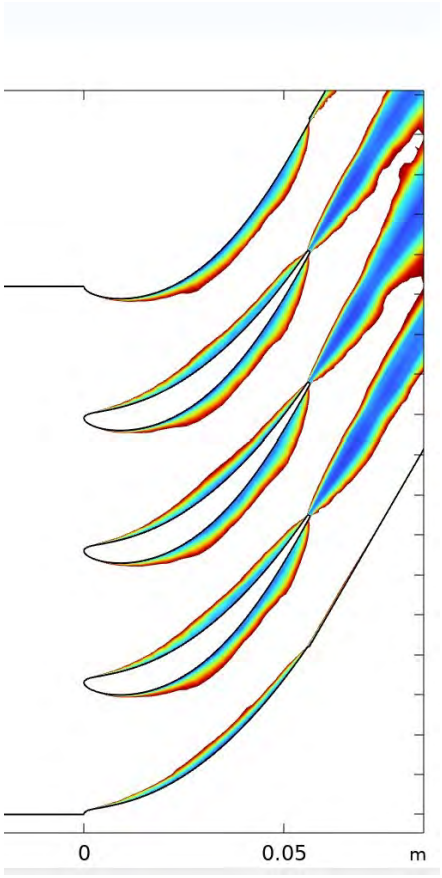

Figure 4.2: closeup

Immediately, it is clear that the mesh prism layers at the boundaries in these early runs would not be sufficiently dense for 3D LES (this much was expected as these were not even dense enough for accurate wall treatment in 2D RANS). What was surprising, however, was that repeating this after the wake refinement done at this early stage almost completely eliminated the unrefined areas in the rest of the domain as seen in Figure 4.3:

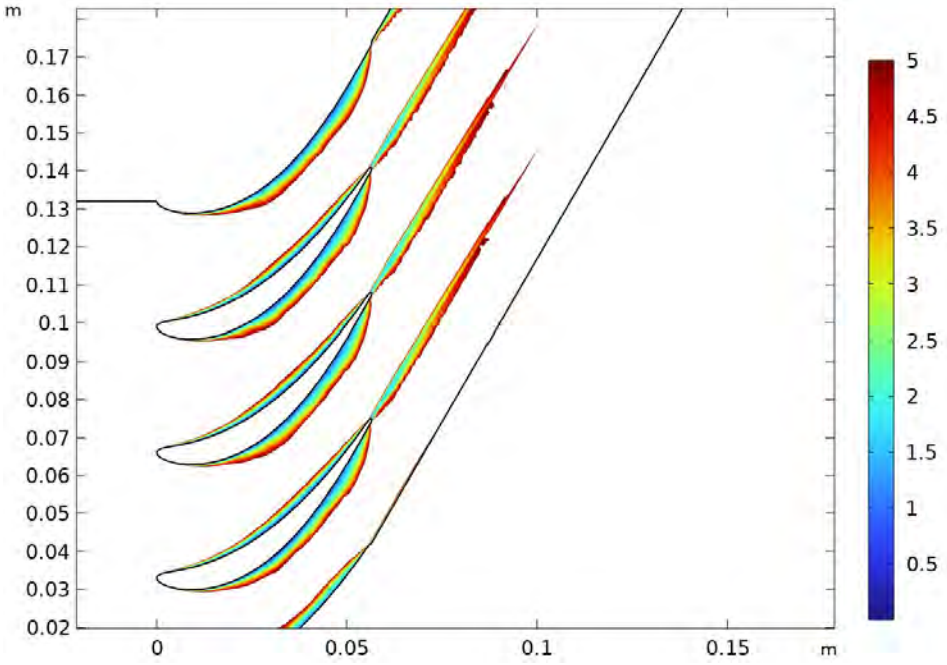

Figure 4.3: Closeup of areas with $f_{fineness} < 5$ after wake refinement

Proving that wake refinement will be a very powerful refinement tool and should be the first approach for mesh refinement before 3D LES (after adjusting prism layers to a $y+$ adequate for LES).

4.2 2D GCI

To prove that 2D flow results are free of discretization errors, a GCI calculation was conducted across three different meshes with varying quality. The representative solution value (ϕ_i) for the GCI was static pressure ratio. All three meshes were generated in COMSOL where the average cell length h_i from each mesh could be extracted by doing an average evaluation of the square root of COMSOLs internal expression meshvol. The number one represent the finest mesh, two the medium mesh and three the coarsest mesh. The representative solution values and average cell lengths of each mesh can be seen in Table 4.1 below:

Table 4.1: First set of values for GCI

Mesh nr	h_i	ϕ_i
1	0.0014149	1.2334
2	0.0022084	1.2344
3	0.0034775	1.2378

The respective grid refinement ratios is then $r_{32} = 1.574669444$ and $r_{21} = 1.560817019$, which is more than sufficient for the $r \geq 1.3$ requirement for GCI. The respective solution differences are $\epsilon_{32} = 0.0034$ and $\epsilon_{21} = 0.001$. This gives an $s = 3.4$. With the equations for p in Equation 3.9 and q in Equation 3.10 both have two unknown variables at this point, that being p and q, they were put together in a matlab script to compute that $p = 2.753996$. Now that all the values for equation 3.11 are acquired, the result is:

$$GCI_{21,fine} = \frac{1.25 \left| \frac{\epsilon_{21}}{\phi_1} \right|}{(r_{21})^p - 1} = 0.00042088387 \approx 0.0421\% \tag{4.1}$$

A GCI of ≈ 0.0421% is very low, well below typical target thresholds. This means that results produced through use of the fine mesh are grid independent and purely driven by the physics in the domain, though it also means that the mesh may be a little bit too fine, using excessive computational resources for simulations.

4.3 2D Validation

Validation of the 2D flow results was done by setting the 2D model to cruise conditions found in the E^3 LPT performance report [1], and relevant result parameters chosen to compare to those found in that same report. This should provide some confidence that there are no setup errors in the 2D simulations of this study. As mentioned in Section 3.8 there are no LPT results for the hot day takeoff values used so this was seen as an acceptable validation.

With cruise conditions, the total pressure goes from 255000Pa to 250110Pa across the domain which can be seen in Figure 4.4. This gives a total pressure ratio ($P_{tot,out}/P_{tot,in}$) of 0.981. That is very close to the total pressure ratio from [1] performance report at pitchline, which can be seen in Appendix A.8.

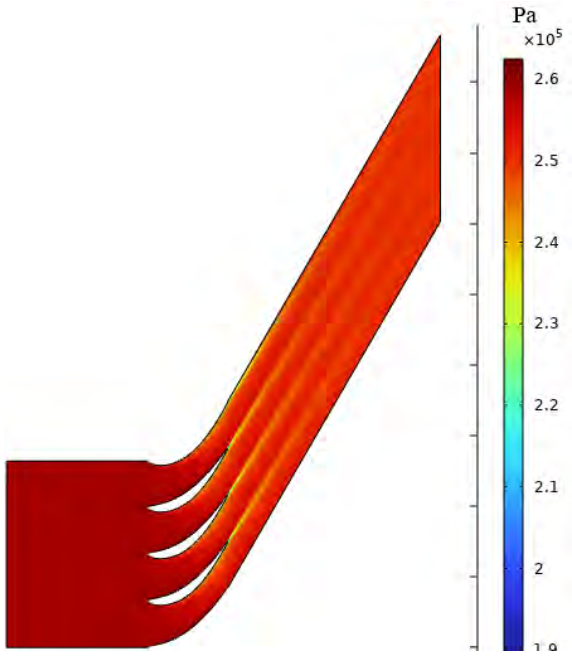

Figure 4.4: Total pressure across domain at cruise

The velocity flow angle was measured at the outlet of the stators in Figure 4.5. The flow angle was measured to be between $59.2261°$ and $59.7109°$. This is close to values from the performance report [1] at pitchline. These can be seen in Appendix A.7.

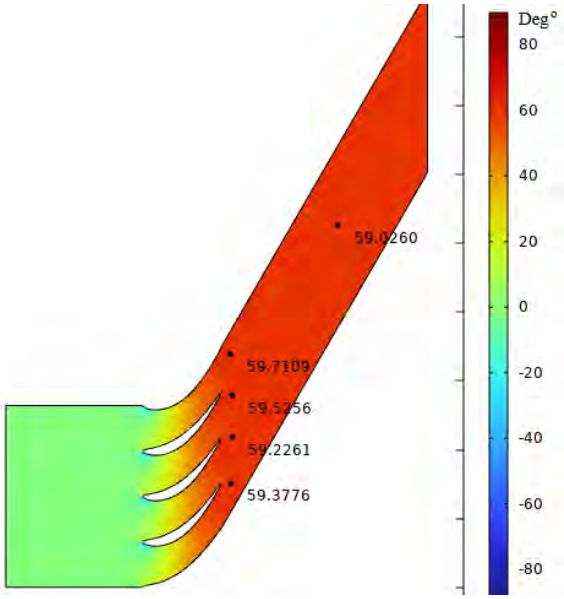

Figure 4.5: Velocity flow angle at stator outlet

In Figure 4.6 specific points around the pressure and suction sides of stator vanes from NASA test data [1] (full plots in Appendix A.6) are plotted and compared to the same points in the cruise simulation.

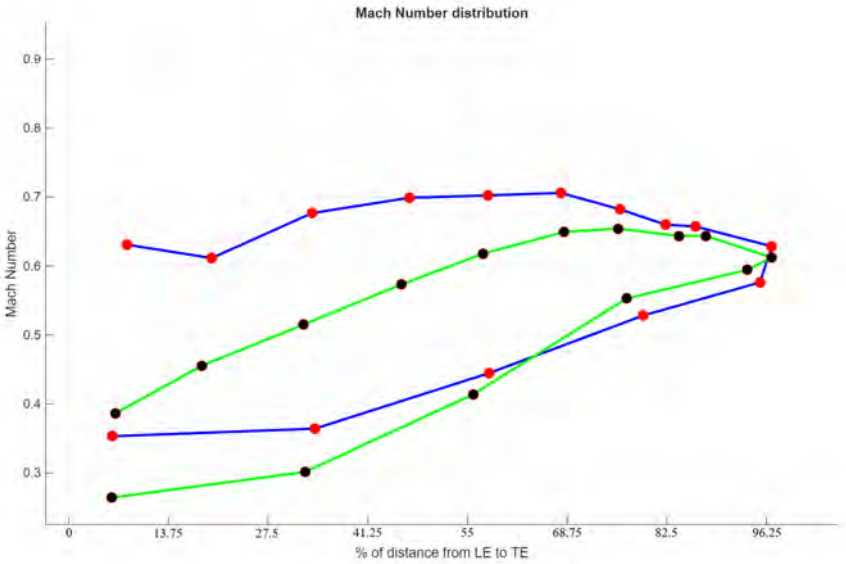

Figure 4.6: Mach Number distribution around the stator. Blue line and red dots are from [1], while green line and black dots are from the COMSOL cruise simulation

The local Mach numbers near stators generally line up well between testing and simulations. However, towards the leading edge, some disparity appears.

The divergence in leading edge values could be due to a variety of reasons. The first pressure tap on the suction side could be an aberration; the cubic interpolation of those points in the original documentation is definitely closer to the COMSOL data (original in Appendix A.6 and CFD data in green in Figure 4.6) and suggests as much. The comparison is also not perfect due to the fact that the original testing pressure taps were on a horizontal 50% cut of the stators, while all 2D simulations were done with a slightly angled pitchline.

The metrics of Total pressure ratio, outlet flow angle and Mach Number distribution from the cruise simulation that were selected for validation line up well with results of equivalent metrics found in the performance report [1] and give some confidence to the flow results in non-cruise conditions that are the main focus of this study.

4.4 2D Flow Results

Stationary flow simulations took around 20 minutes to converge, where the physics model paired with the coarse mesh was first simulated to use its results as initial values for the physics model with the finer mesh. Although the mesh cell count and boundary layers differ a lot in quality, the resulting flow results are identical for both.

Velocity decreases to ≈ 170m/s by the time the fluid reaches the stators where it then rapidly increases to ≈ 400m/s through the stators as can be seen in Figure 4.7. In Figure 4.8, streamlines curve around the stator walls all the way to the T.E where the flow eventually reconnects as expected.

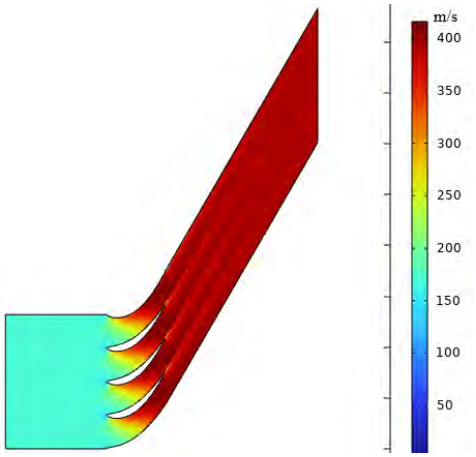

Figure 4.7: Velocity throughout domain

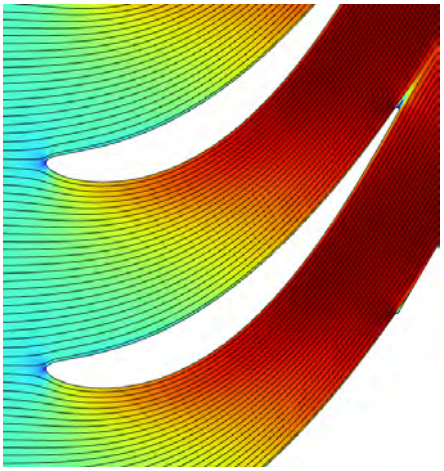

Figure 4.8: Streamlines around stators

The total pressure is 829720Pa at the inlet, this equates to a inlet static pressure of ≈ 799290Pa, as can be seen in Figure 4.9. With the outlet having a static outlet pressure of 648218Pa, as mentioned in the methodology, the static pressure ratio over the stators ($P_{stat,in}/P_{stat,out}$) becomes 1.233. Total pressure at the outlet is ≈ 811430Pa which equates to a total pressure ratio ($P_{tot,out}/P_{tot,in}$) of ≈ 0.98, which is in line with modern turbine stators.

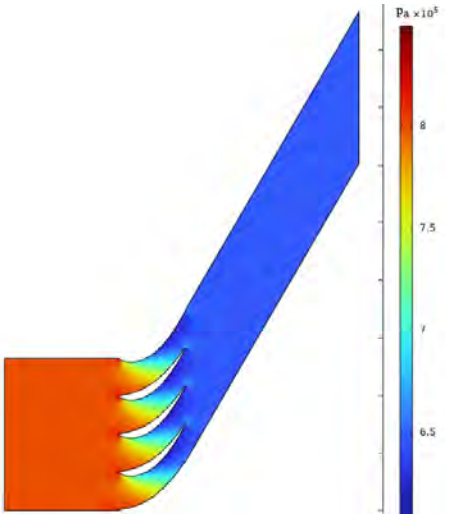

Figure 4.9: Static pressure across domain

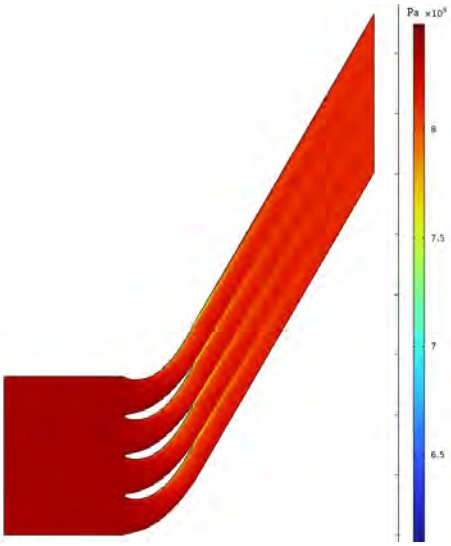

Figure 4.10: Total pressure across domain

At the inlet of the domain, static temperature is measured to be 1107.5K. Throughout the domain, static temperature drops to 1053.5K, giving it a static temperature ratio of ($T_{stat,in}/T_{stat,out}$) ≈ 1.051 which is reasonable. Since the stators are stationary, they do not perform any mechanical work on the fluid and thus the total temperature remains almost completely constant throughout.

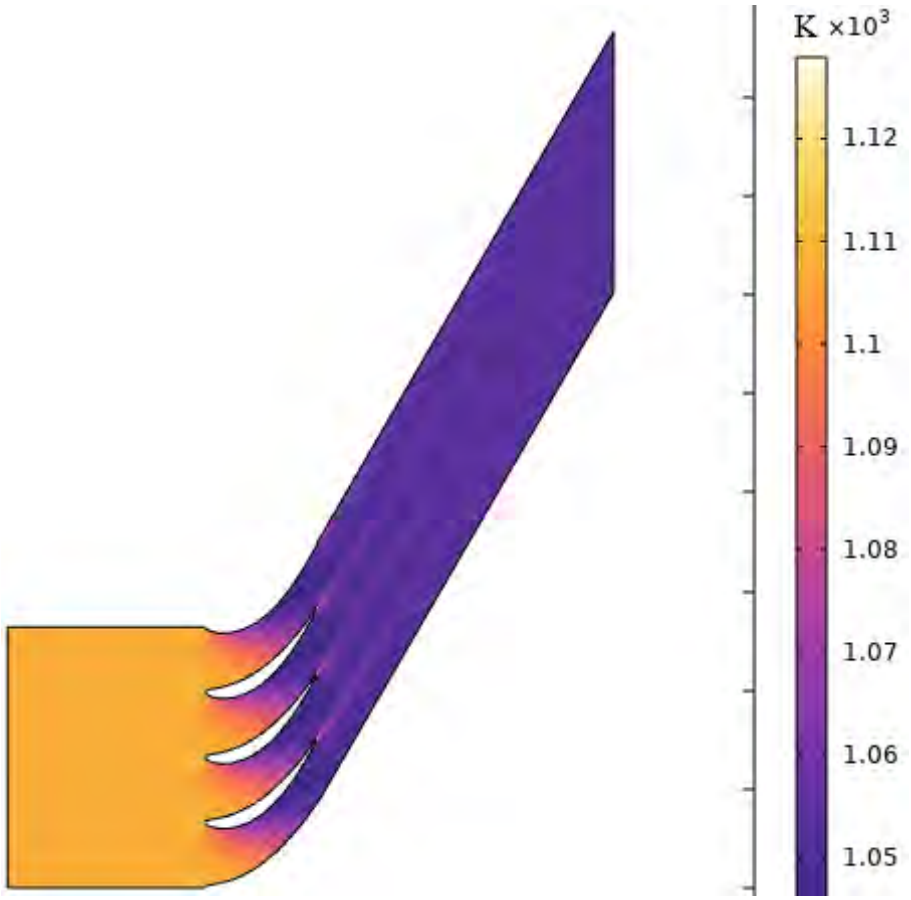

Figure 4.11: Static temperature across domain

Since this is considered a highly compressible flow, the density in the fluid decreases significantly. Figure 4.12 shows a fluid density of $2.51472\text{kg}/\text{m}^3$ before the stators close to the inlet and a density of $2.14002\text{kg}/\text{m}^3$ after the stators close to the outlet. This represents a density change of $\approx 14.9\%$, this is further discussed in section 4.6.

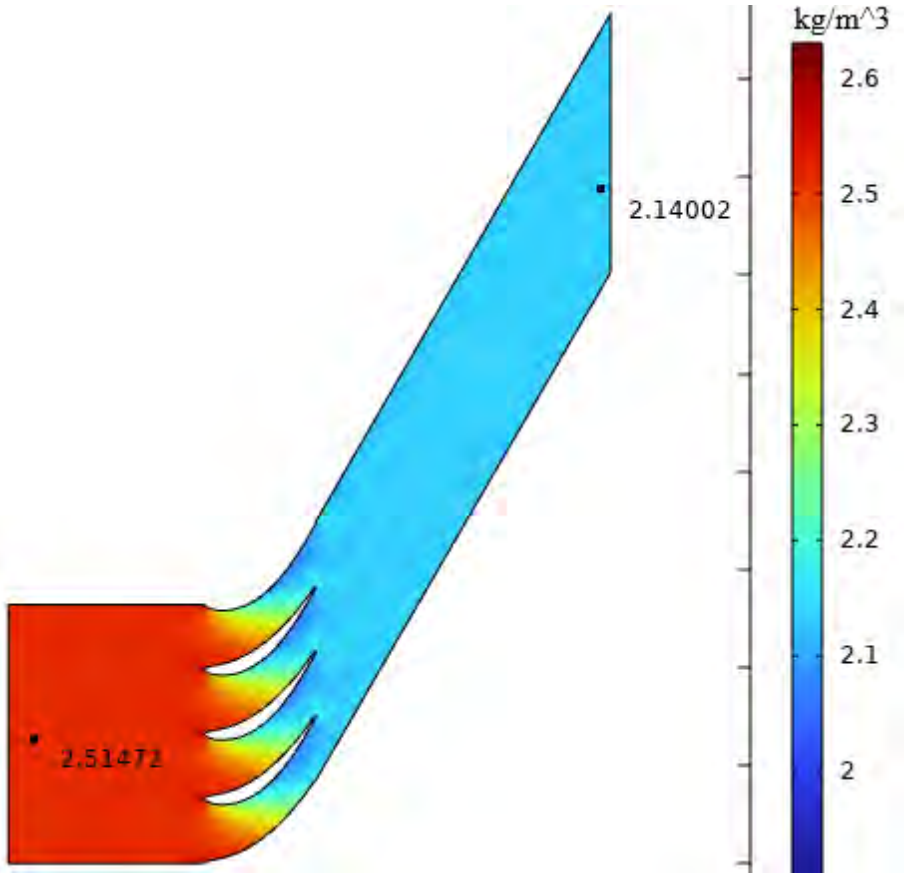

Figure 4.12: Density across domain

As mentioned in the methodology, inlet Mach was set to 0.273. Figure 4.13 shows a mach number between 0.62639 - 0.63792 right at the outlet of the stators. This correlates very well with performance tests conducted on the E^3 LPT in [1], where in Table IV their stator exit mach number at the pitchline was 0.633. Toward the outlet of the domain, after the freestream fluid has had time to mix with the small mach number regions produced at the stator T.E, the mach number is between 0.61485 - 0.61829.

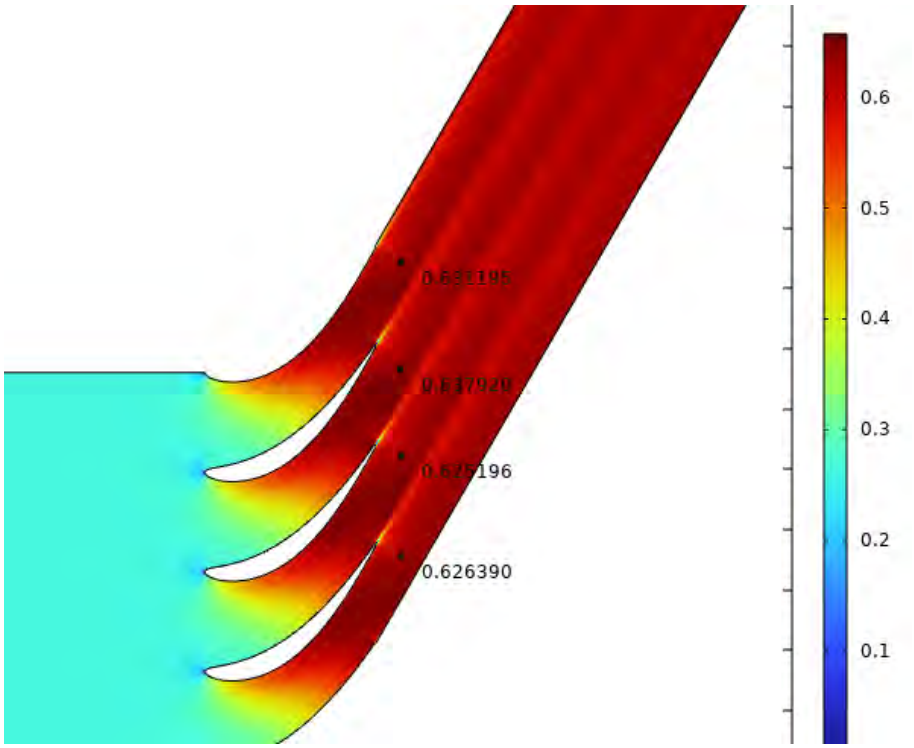

Figure 4.13: Mach number at stator outlet

Flow results are summarized in Table 4.2.

Table 4.2: Flow result summary

Velocity change	$\approx +230\text{m/s}$
$P_{stat,in}/P_{stat,out}$	1.233
$P_{tot,in}/P_{tot,out}$	1.0225
$T_{stat,in}/T_{stat,out}$	1.051
$T_{tot,in}/T_{tot,out}$	1
Change in density	14.9%
Stator outlet mach	0.62639 - 0.63792

4.5 2D Runs with Chemistry Coupling

The time dependent simulation with chemistry coupling took around 16 minutes to reach convergence. After this was completed, both 2D surface plots and 1D line plots were generated on areas of interest.

In Figure 4.14, you can see the change in NO molar concentration (X_{NO}) occurring throughout the domain. The values depicted on the colorbar are in the units mol/m^3. Concentration remains at a constant $X_{NO} = 0.020946$ mol/m^3 right up until the stators. This is where concentrations starts to rapidly decrease until eventually evening out at $X_{NO} \approx 0.017816$ mol/m^3 after the stators. This behavior is consistent with the fact that all flow related parameters undergo drastic changes in that same region around the stators.

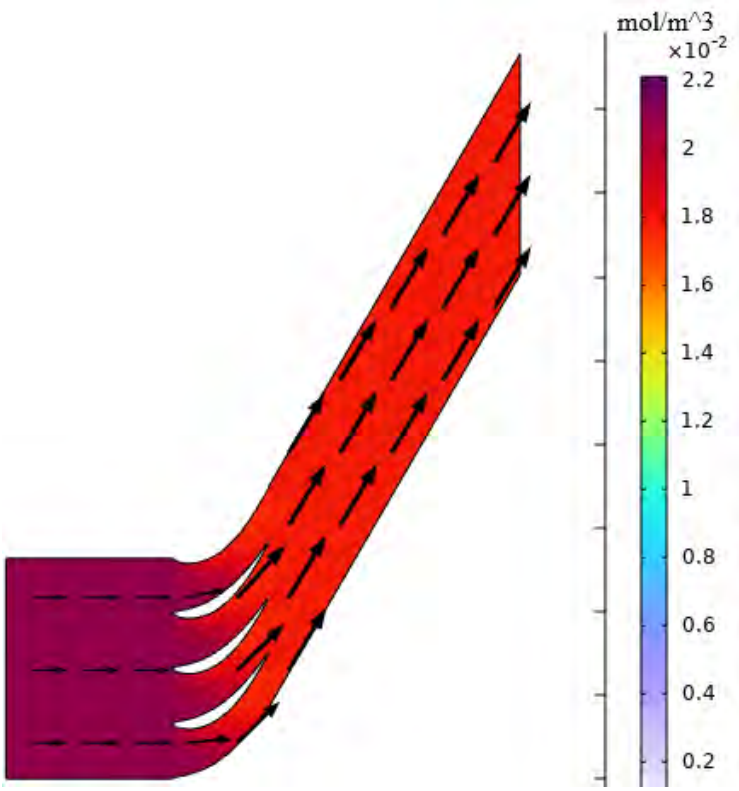

Figure 4.14: Change in NO molar concentration X_{NO} across domain in the units mol/m^3, arrows display NO molar flux.

For plotting the NO conversion throughout the time dependent study, an average value for NO concentration (X_{NO}) was taken from from the inlet and outlet of the domain and put through the equation 4.2.

$$\%X_{NO} = 100 \cdot \frac{X_{NO,in} - X_{NO,out}}{X_{NO,in}} \tag{4.2}$$

The resulting plot of this equation can be seen in figure 4.15.

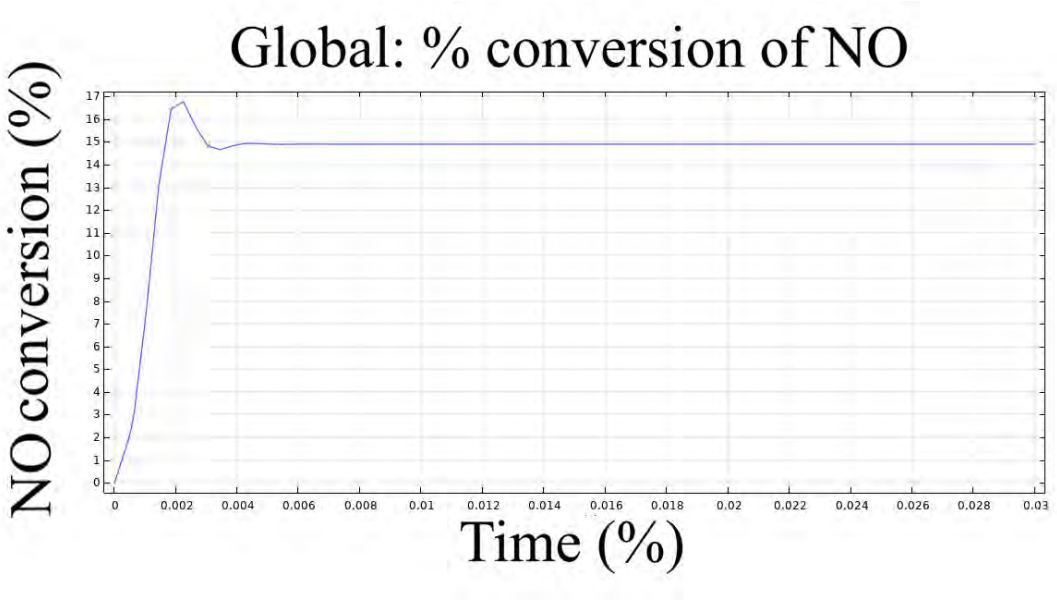

Figure 4.15: $\%X_{NO}$ of time dependent study, displaying a 14.786% conversion

At first glance, a concentration change of 14.786% seems very good. However, a parametric sweep of TOF was conducted where the reference TOF was multiplied by factors between zero and 100 using the same equation for NO conversion as in Figure 4.15. Results of this sweep can be seen in table 4.3:

Table 4.3: Parametric sweep of TOF for $\%X_{NO}$

TOF multiplier	$\%X_{NO}$
0	14.692
0.01	14.693
0.1	14.702
1	14.786
10	15.624
100	24.006

Although the behavior of the $\%X_{NO}$ in relation to varying TOFs is in line with observations from previous work [7], a reference TOF multiplied by zero, effectively disabling the TOF should mean that the catalytic conversion in the system becomes zero. However, that was not the case for this sweep. This indicates that something is inherently incorrect with the chemistry coupling. This is discussed further in section 4.6.

4.6 NOx Conversion Measurement Inadequacy

The conversion rate with the more accurate compressible flow model seems exceptionally high when compared to previous work [7]. This suggests that the apparent conversion might be a postprocessing artifact or may arise from an inconsistency with the modeling setup.

To test this hypothesis, the same measurement method used for conversion was used for density percentage change as follows:

$$\%\rho = 100 \times \frac{\rho_{int,1} - \rho_{int,2}}{\rho_{int,1}} \tag{4.3}$$

with $\rho_{int,1}$ being the density averaged over the entire inlet and $\rho_{int,2}$ being the density averaged over the entire outlet. When plotting this result, the problem becomes apparent:

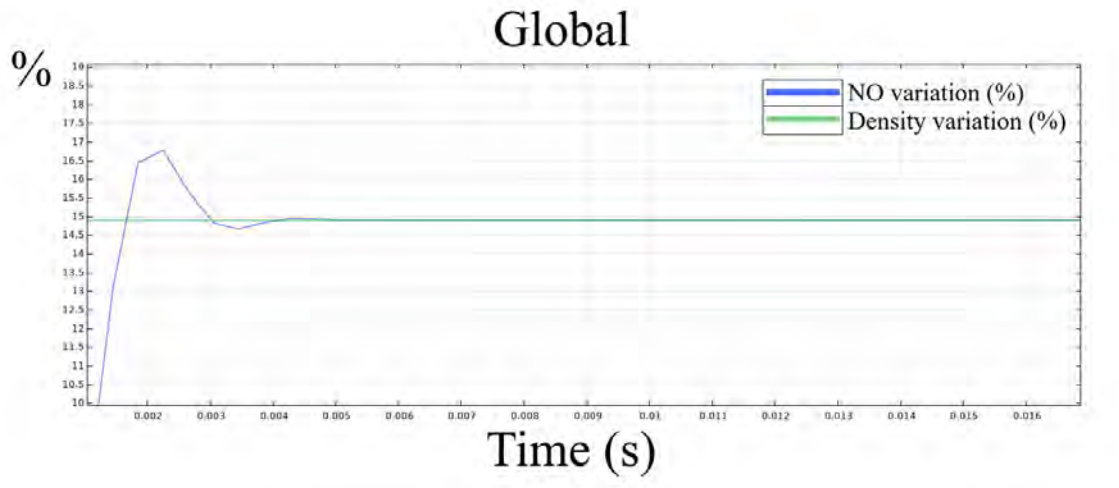

Figure 4.16: Zoomed in $\%\rho$ (in green) and $\%X_{NO}$ (in blue) over simulation time

The conversion seems to almost match the density variation from inlet to outlet (note that the density plot is obtained from the stationary compressible fluid flow so it is obviously steady, while the coupled chemistry simulation is time dependent).

The chemistry models that were used, use concentration percentage change, which is standard in catalysis modeling. However, the concentration of a species i, c_i, can be written as:

$$c_i = \frac{\rho_i}{M_i} \tag{4.4}$$

where M_i is the molar mass of the species and ρ_i is its density, which is related to the total mixture density through the mass fraction, meaning that changes in total density can change the molar concentration even if no chemical conversion has occurred. In most catalyst modeling cases, this would not be a problem, as Reynolds numbers are low, and the fluid flow can be modeled as incompressible.

The flow in this study cannot be classified as incompressible, and the compressible models used lead to a density variation, which while being more accurate to the real flow, leads to a variation in NO concentration that does not reflect an actual conversion.

To solve this, a new conversion measurement method is proposed: instead of concentration, NO molar flux variation can be used. Molar flux of a constituent i, N_i (mol/m$^2\cdot$ s), gives a measure of the actual number of moles of the constituent that pass through a square meter of a boundary every second.

Averaging for inlet and outlet and converting to percentage:

$$\%N_{NO} = 100 \times \frac{N_{NO,in} - N_{NO,out}}{N_{NO,in}} \tag{4.5}$$

Plots for $\%X_{NO}$ and $\%N_{NO}$ for the original coupled model results (from previous work [7]) are presented in Figures 4.17 and 4.18

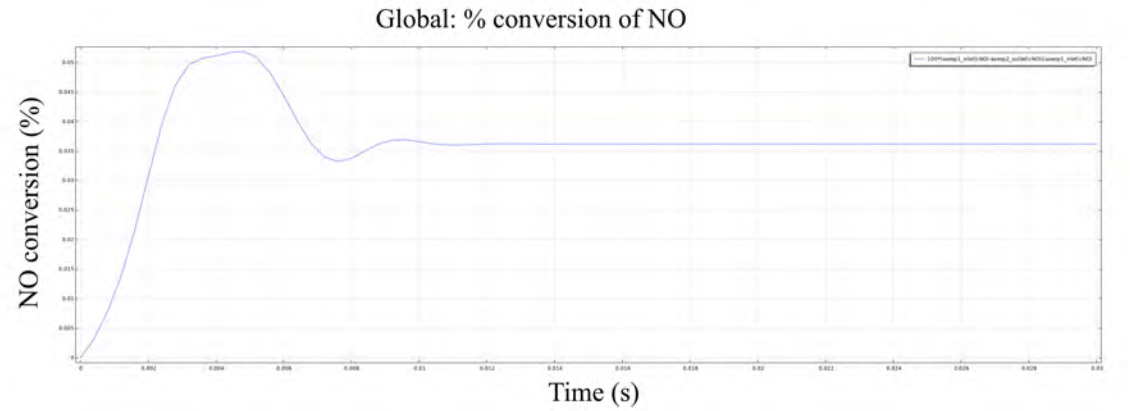

Figure 4.17: $\%X_{NO}$ plot from the previous work (stabilizes at 0.036%)

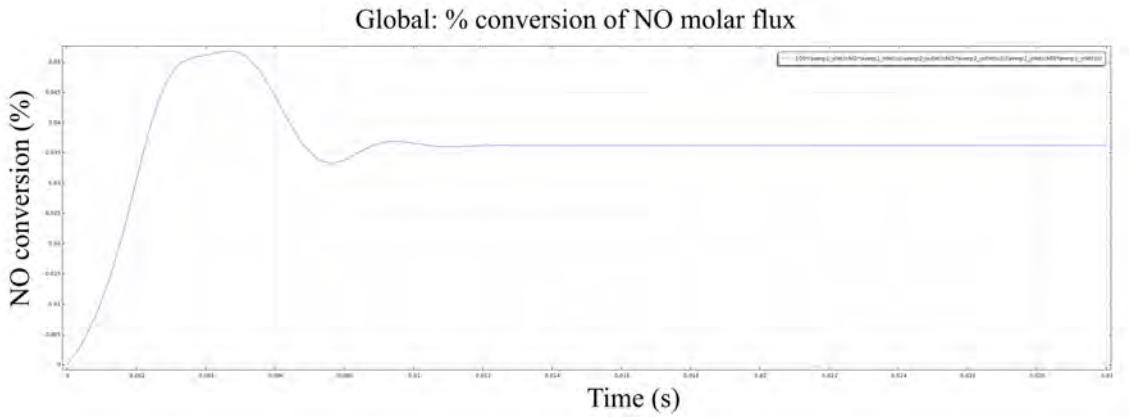

Figure 4.18: $\%N_{NO}$ plot from same results (stabilizes at same values and behaves the exact same)

As expected, molar flow percentage difference is exactly equal to the concentration percentage difference since the flow models used were incompressible and, as such, using concentration as a tool to measure NO conversion is adequate as is the case in most catalyst modeling cases.

However, plotting molar flux variation for the coupled surface chemistry and compressible flow results in this thesis (Figure 4.19) completely changes the results, stabilizing at 0.0132%, making them significantly closer to previous results [7] and supporting the idea that molar flux is a more adequate tool for a catalyst in a compressible flow.

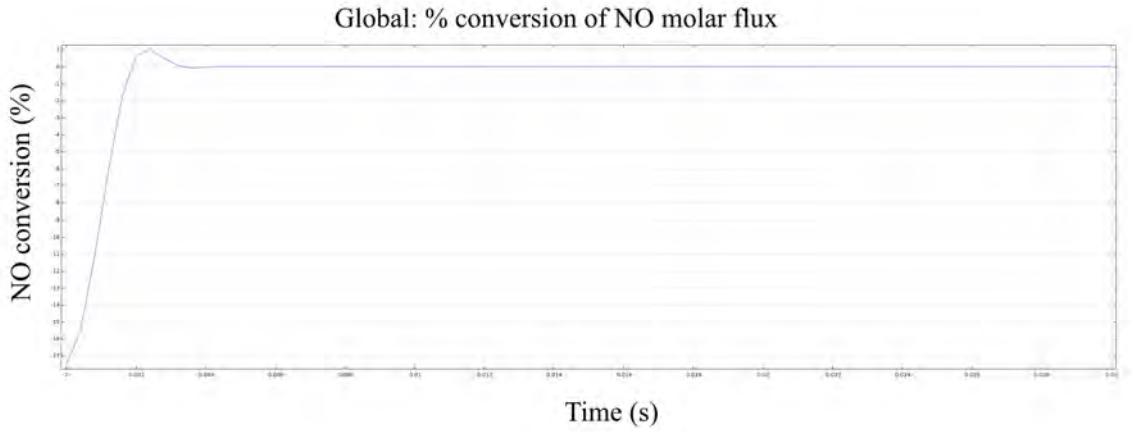

Figure 4.19: NO conversion in molar flux ($\%N_{NO}$)

4.6.1 Alternative NO_X Conversion Measurement Method and Partial Pressures

For the chemistry coupling used in this thesis and in previous work[7], the partial pressures used to scale TOF were fixed at constant values. Realistically, that is not the case. Partial pressures in the domain should be dynamic, dependent on local pressures instead. This was implemented to perform a parametric sweep of TOF but this time plotting molar flux N_{NO} instead.

Table 4.4: Parametric sweep of TOF for $\%N_{NO}$ with dynamic partial pressures

TOF multiplier	$\%N_{NO}$
0	0.001
0.01	0.0011
0.1	0.0021
1	Not converged
10	Not converged
100	Not converged

Unfortunately, the solver started diverging around TOF multiplier of one with dynamic partial pressures. Reaching residuals of 10^{150} before the simulations were terminated and this sweep could therefore not be completed. That same parametric sweep but with previously mentioned constant partial pressures instead looks like in Table 4.5 below:

Table 4.5: Parametric sweep of TOF for $\%N_{NO}$ with constant partial pressures

TOF multiplier	$\%N_{NO}$
0	0.001
0.01	0.0011
0.1	0.0022
1	0.0132
10	0.1226
100	1.2171

4.7 Preliminary 3D Runs

Due to time constraints and severe convergence issues, 3D runs where not finalized but the process is still of some interest for future work. For these reasons, this section will delve deeper into the process and the challenges faced.

4.7.1 Special Considerations with Meshing

When meshing, an "identical mesh" constraint was used (see Section 3.4.1) which ensures periodicity, but can lead to significant problems with over constraining. Any constraints on edges of the periodic boundaries will lead to problems. Looking at a concrete example, below is an early 3D mesh seen from the top i.e. looking at a slice of the LPT casing where it intercepts with the stator vane and with the edges that are shared between the periodic walls and the casing highlighted in blue:

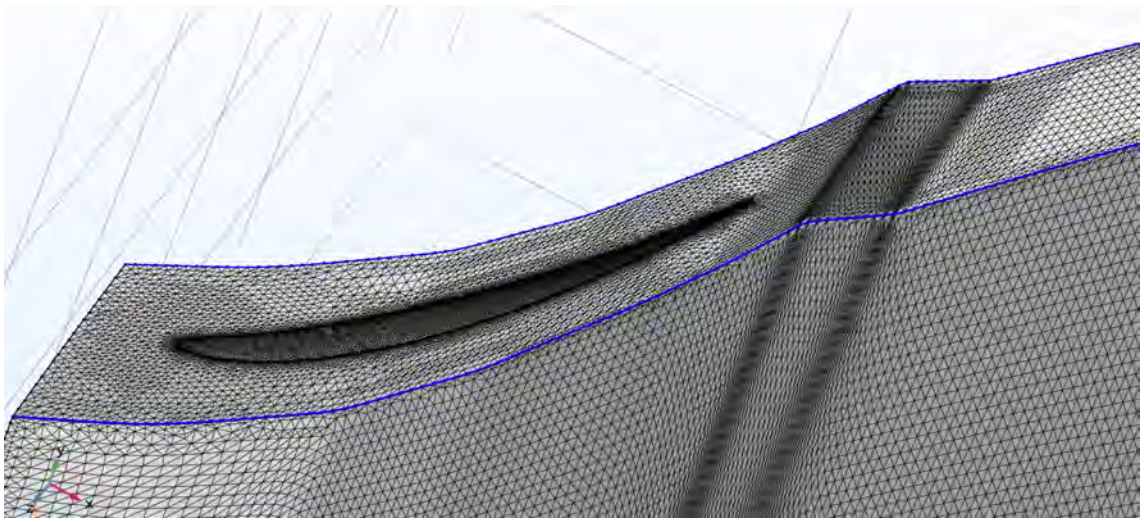

Figure 4.20: Closeup of the early casing mesh with casing-periodic edges in blue

The first approach, as in 2D, was to manipulate the 2D mesh of each face through the settings of the free mesh on the face and "distribution" constraints on its edges. This almost always lead to a failure of the identical mesh.

The correct approach, counter-intuitively, was to apply all edge constraints that are shared with the identical mesh faces asymmetrically and only on the side that is used as the "source" for the identical mesh. The identical mesh then leads to this distribution being applied on the other edge as well. In the case of Figure 4.20, only one of the highlighted edges (on the identical mesh "source" side) has a "distribution" constraint applied, but the end result is the same distribution on both edges. The same workflow had to be used for every face except the stator walls (as the stator vanes do not share edges with the side walls).

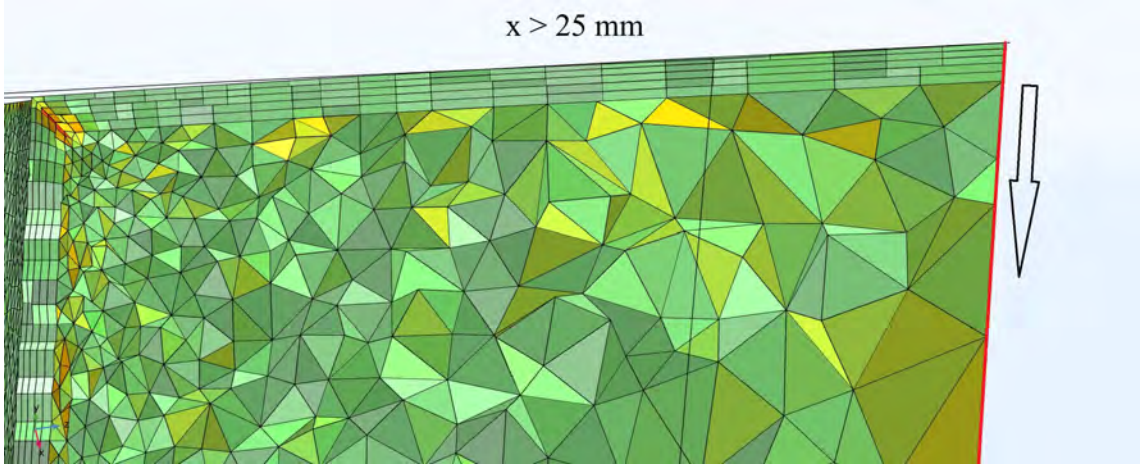

Figure 4.21: Closeup of a later 3D mesh cut at $x = 25$mm showing stator and casing boundary layer connection (periodic boundary in red)

The same over constraint problems also affect boundary layer meshing. COMSOL handles boundary layers by generating prismatic layers as usual and then deforming the free tetrahedral mesh (free triangular in 2D) to "fit" said prismatic layers. In turn, the transition to the rest of the mesh is smoothed through an iterative process. This iterative operation, when part of the affected mesh is shared by the "identical mesh" constraint and caused problems frequently. The only way found to produce a smoothed transition that did not cause the identical mesh to fail was to limit "maximum element depth to process" (shown in figure 4.21 as an arrow for the LPT casing boundary) to 1 mesh element and increase the number of iterations for the transition operation.

4.7.2 Sweeping Velocity Inlet Conditions Around A Center of Rotation

Setting velocity conditions for the inlet was very straightforward in 2D but became an unexpected hurdle for 3D. As mentioned in subsection 3.4.2, the velocity field was an interpolated function with blade height as the input (see Figures 4.22 and 4.23). As the domain is a section of an annulus, simply using the z coordinate as the input would be inaccurate and there was a lack of similar cases done in COMSOL to use as a guideline.

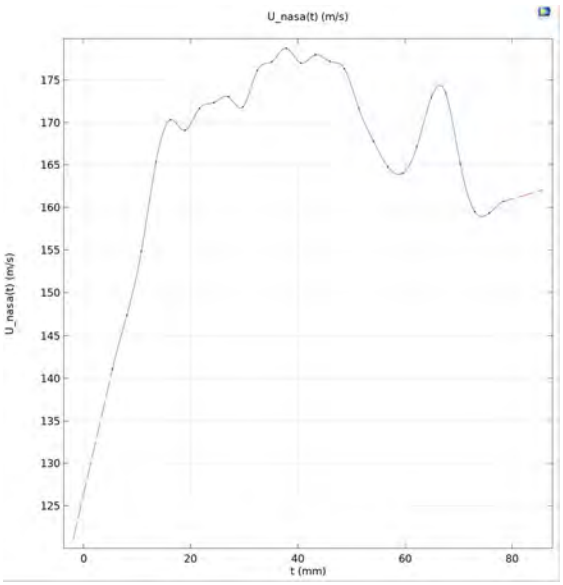

Figure 4.22: Interpolated axial velocity field

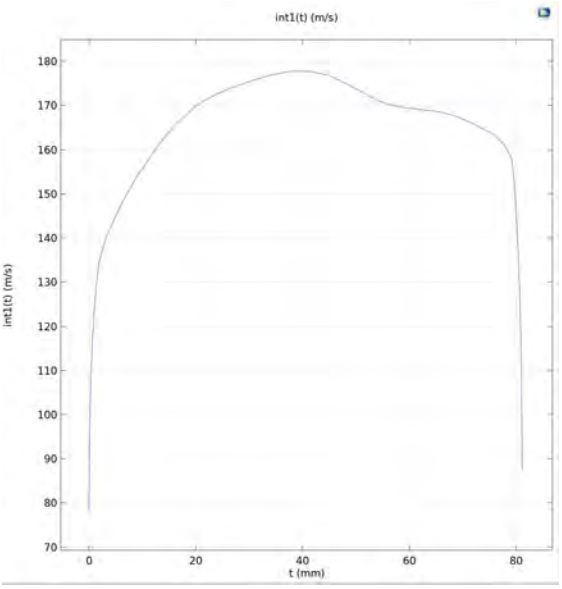

Figure 4.23: Axial velocity with boundary layers

The solution found was to create a second coordinate system in addition to the global cartesian coordinate system. This cylindrical system had its origin on the centerline of the engine (while the global coordinate system has its origin at the inlet) and can then be used as the input for the velocity fields. Figure 4.24 is an example of the setup used in an early run with no boundary layers for troubleshooting and the resulting inlet velocity field is presented in Figure 4.25(notice that for axial velocity it is enough to use radius as the input and subtract r_{hub} but radial velocity also has to be converted into cartesian coordinates).

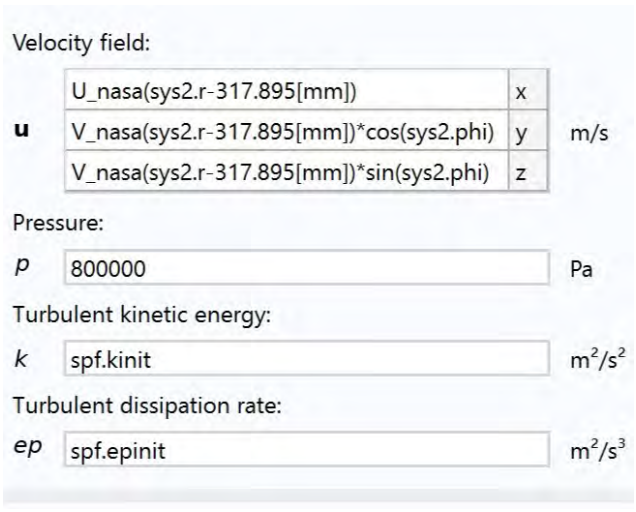

Figure 4.24: Early inlet setup in COMSOL (axial velocity field U_{nasa} and radial velocity field V_{nasa})

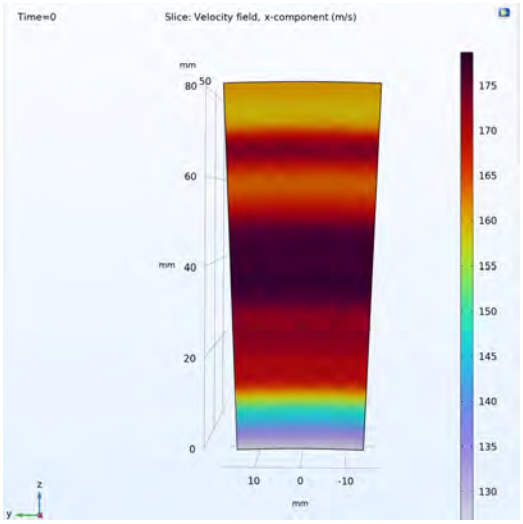

Figure 4.25: Curved banding in inlet suggests the setup is working as intended

4.7.3 Convergence Issues

For 3D runs, convergence was a significant challenge. The current working hypothesis is that there is a fundamental mismatch between the inlet conditions and the geometry of the fluid domain.

During the 3D simulation process, it became apparent that the high-fidelity NASA simulations from which the inlet data was obtained did not include the HPT-LPT duct as this wasn't relevant for that study case, and, as a result, the supposed inlet conditions used in this study are not strictly LPT inlet conditions, but rather HPT exit conditions.

As COMSOL is an FEM instead of an FVM solver, it could be more unforgiving when it comes to setup; where one could get away with an unrealistic setup in an FVM solver, an FEM solver user will be faced with non values in velocity and turbulence matrices. Plotting the velocity field (with the method from subsection 4.7.2) and the hub and casing wall seems to support this hypothesis. For an LPT inlet, it would be expected that the velocity field near a wall be in the same direction as that wall when this is clearly not the case for these inlet conditions (see figure 4.26)

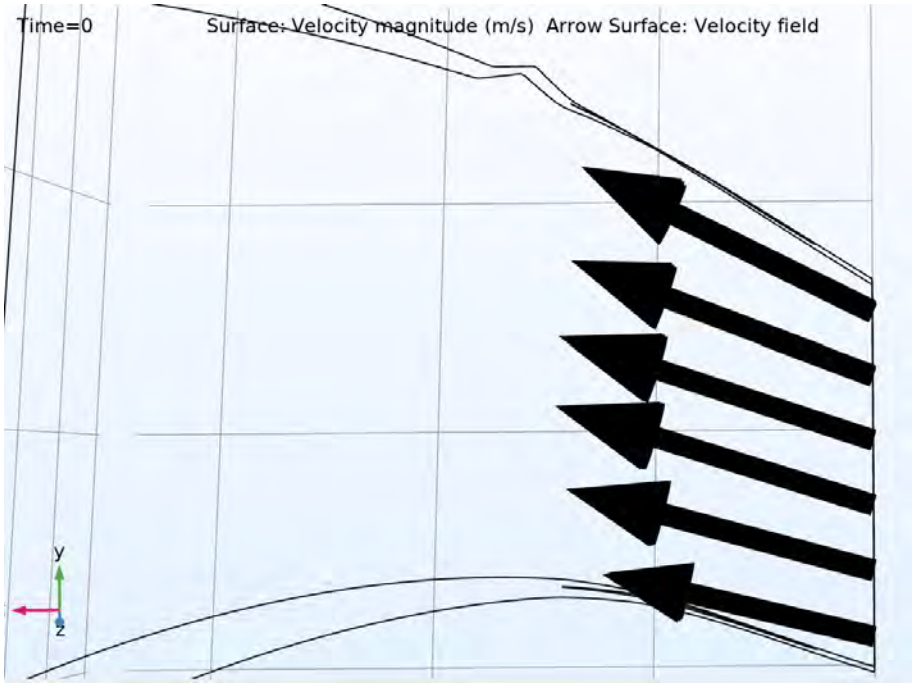

Figure 4.26: Inlet velocity field with accurate velocity directions but vector length increased to aid visualization

During troubleshooting, simply neglecting radial velocity, and making inlet flow fully normal (i.e. using the axial velocity field only) was not successful in obtaining convergence. Figure 4.26 confirms that, assuming that the problem comes from flow-walls misalignment as was hypothesized, the problem will only be made worse on the hub with a purely axial flow.

4.8 High Performance Computing Cluster, Vera

COMSOL has scalability issues, especially in 3D. To allow for a faster turnaround between simulations and reasonable simulation times, Chalmers allowed for Vera and other super-computing resources to be used.

Running on Vera was very straightforward, with access through SSH and COMSOL being able to run in batch mode by default.

The generic bash script used to run COMSOL on Vera can be seen in the Appendix (figure A.5). COMSOL is a CPU bound software and is programmed to automatically utilize all available hardware on a compute node through an MPI controller. For this reason the entire node is booked and the script demands all 64 cores of a Vera node to operate at peak efficiency.

There were two main drawbacks with using COMSOL in a batch. Since COMSOL's iterative solvers are very RAM efficient and simulations were split into a stationary step to solve the fluid flow and a time-dependent step to study the concentration-reaction transport, jobs often never exceed 100 out of the standard 768 GB of RAM in a node. This leads to jobs not taking advantage of the incredibly high RAM available in a super-computer node while still being relatively expensive (as usage is commonly measured in core hours and all available cores in a node were used). This can be seen clearly with Vera's excellent job monitoring tool; in Figure 4.27 is the performance of a COMSOL job where meshing was already done before submitting. The job consistently used the 64 cores demanded by the bash script and spent over 220 core hours but RAM usage never exceeded 30 GB.

Figure 4.27: Typical COMSOL batch job performance without meshing

Another disadvantage that became apparent is the fact that meshing is locked to one core per domain which, in the geometries in this study, leads to only one

core being used. This results in meshing speeds on Vera comparable to those of a home computer as the only relevant factor is the per core performance. This also makes multigrid methods, where a coarser mesh is used to help with convergence, not nearly as effective. See Figure 4.28 for the performance of a relatively simple coupled chemistry run without meshing previously. Even though the job was extremely fast, nearly a third of the computing time was used on meshing on one core only (which still counts as 64 cores in terms of core hours as these cores are reserved).

Figure 4.28: Performance for a job that included meshing (meshing from around 14:05:30 to 14:08:30)

5
Future work

5.1 CFD Recommendations

The primary focus for future work, from a CFD standpoint, should be on obtaining accurate unsteady 3D flow results and coupling them with surface chemistry. There is good reason to believe that sections with lower flow velocities near walls and with high separation such as the gap for seals in the turbine casing will promote better conversion rates [7]. Furthermore, in 3D, the catalytic alloy will be present on the hub and casing of the stationary section of the LPT instead of just the stator vanes, disproportionally increasing the surface area from 2D to 3D and previous work [7] shows that conversion is strongly correlated with the coated surface area. Lastly, there are significant unsteady effects in an E^3 engine LPT [18] that are not present in 2D or stationary 3D simulations, and these could significantly affect near-wall flows and, consequently, catalyst performance.
For these reasons, it is appropriate to assume that one does not have a complete enough picture of the influence of the flow on NOx conversion unless these higher fidelity simulations are performed.

To solve the inlet field problems described in subsection 4.7.3, which are assumed to be one of the main culprits of the 3D convergence issues, a couple different approaches are proposed:

- Create an educated guess for a more acceptable inlet velocity field with reasonable assumptions from the wide array of literature available for the E^3 engine. This would obviously have less validity than directly using test data but, as this work is at a proof of principle stage, it could be seen as an acceptable compromise.
- Begin again at the 3D modeling stage (section 3.3) for a corresponding $1/72$ slice of the HPT-LPT duct and run flow simulations using HPT exit conditions to obtain more accurate inlet conditions for the 3D domain that was modeled and simulated in this study.

Also of note is the possibility of using an FVM solver due to its robustness and ease of simulating more unstable flows. A software with an FVM solver, such as Star-CCM+, for example, could be used at a troubleshooting stage for faster turnaround times and being faster at achieving a complete picture and understanding of the flow. FVM results could then be used as initial conditions or even as the final RANS results, as COMSOL is fully capable of importing a flow from a different mesh and interpolating it for its own mesh. COMSOL would then be used for the LES, multiphysics, and chemistry phases of the process.

5.2 Surface Chemistry Recommendations

From the results of this thesis, it has become apparent that the setup for the chemical coupling is not adequate enough to produce reliable results and will need to be looked at further. The method on how to accurately measure and plot NO conversion will need to be investigated further. Whether change in concentration (mol/m^3), as is standard for low velocity catalysts, change in molar flux (mol/m^2·s), molar flow rate, or a comparison between a reference run and a test run (one with no chemistry and another with coupled chemistry) would be a more ideal measurement tool.

Inlet parameters for the chemical coupling in this thesis were imported from previous work [7] due to time constraints. These to be looked at and adjusted.

Dynamic partial pressures needs to be implemented to get a more realistic view of local concentrations in the domain. It is also essential for implementing a correct scaling factor of TOF.

Diffusion boundary layer thickness variable (d) that is used for the volumetric consumption rate ($r_{NO,vol}$) needs to be recomputed. The value for d used in this thesis is set by default in the model from [7], and is closer to an average mass boundary layer thickness as it is understood in fluid dynamics. For a more accurate representation, future simulations could compute a diffusion boundary layer thickness from the Schmidt number relation.

To limit the risk of the $r_{NO,vol}$ affecting NO conversion in the entire domain, the domain can be partitioned so the flow is simulated throughout the whole domain while $r_{NO,vol}$ specifically is only enabled for a domain the size of the diffusion boundary layer.

Alternative configuration of the transport of diluted species interface in COMSOL could be investigated. In its current form, a flux node is applied to stators where local wall flux (J_{NO}) of each species are applied with a manually entered equation. Options could be explored to instead use a surface reactions node where COMSOL computes local wall fluxes in-house.

With these changes done to the chemical coupling, the solver will need to be reconfigured and tuned to tackle convergence issues. If issues persist, alternative solvers better suited for this kind of instability could be looked at as replacements.

6
Conclusion

This thesis attempted to build a framework for coupled CFD and surface chemistry modeling of NOx conversion in a turbofan LPT.

There is a high degree of confidence in the 2D flow results, with several parameters tested matching available testing data. The cruise condition runs done for the purpose of validation also matched well with the E^3 LPT performance report [1].

The GCI studies done in this study with a final $GCI_{21,fine} = 0.0421\%$ and an asymptotic ratio of ≈ 0.998 also show that errors due to discretization are negligible in the final results.

Much of the chemistry setup was borrowed from previous work, which made certain variables outdated and in need of recalculation.
The final NOx conversion in molar flux variation percentage was 0.0132% and the turnover frequency sweeps in table 4.5 affect the conversion as expected when turnover frequency is increased ($TOF \times 1, TOF \times 10, TOF \times 100$) with $TOF \times 100$ resulting in $\approx 1.22\%$ conversion which lends some credence to the results and matches the trend in previous work [7]. On the other hand, lower turnover frequencies no longer affect conversion linearly and, most importantly, zeroing turnover frequency does not lead to an absence of conversion which would suggest a problem. This is almost negligible (for $TOF = 0$, $N_{NO,in} - N_{NO,out} \approx 1 \times 10^{-5}$ mol/m^2·s and the residuals for both flow and chemistry simulations were around 1×10^{-6}) but further investigation is warranted.

As discussed throughout the course of this thesis, and especially in Section 5.2 it has become clear that no concrete conclusion can be drawn about the efficiency of the catalyst. Several modifications must be made to the chemical models to raise confidence in the model and reduce risk of setup inaccuracies before a quantitative analysis can be done.

7

Declaration of AI use

Generative AI such as ChatGPT and Copilot have been used to decode error messages, and to clarify certain topics and settings for COMSOL, although that information has been fact checked afterward. Copilot has been used to generate Matlab scripts.

Bibliography

[1] M.J. Bridgeman, D.G. Cherry, J. Pedersen, “Nasa/ge energy efficient engine low pressure turbine scaled test vehicle performance test,” *NASA-Lewis Research Center*, 1983. CR-168290.

[2] E. M. S. Donald Y. Davis, “Energy efficient engine - flight propulsion system final design and analysis,” *NASA-Lewis Research Center*, 1985. CR-168219.

[3] Didier Hauglustaine, Richard C. Miake-Lye, et al., “Icao caep/12 assessment report: Assessment of the impact of airport emissions on local levels of nox and human health; impacts of cruise emissions of nox on human health; impacts of cruise nox on climate,” *ICAO*, 2024.

[4] Evangelia Maria Thoma, Tomas Grönstedt, Xin Zhao, “Quantifying the environmental design trades for a state-of-the-art turbofan engine,” *Aerospace, Vol 7, Iss 10, p 148*, 2020.

[5] Trung Hieu Nguyena, Phuong Nguyen-Trib, Francois Garnier, “3d modeling of transformation of gaseous pollutants in the high-pressure turbine of an aircraft engine,” *Propulsion and Power research, 9, 1*, 2020.

[6] “Basic research needs for catalysis science to transform energy technologies,” tech. rep., U.S. Department of Energy, Office of Basic Energy Sciences Workshop, May 8–10, 2017.

[7] S. Sherriff, “Modelling high-temperature nox emission control in a low-pressure turbine using coupled computational fluid dynamics and catalytic surface chemistry,” Master’s thesis, University of Strathclyde Engineering, 2026.

[8] “Simscale, "What is CFD - Computational Fluid Dynamics?".” Accessed: 2026-02-23, `https://www.simscale.com/docs/simwiki/cfd-computational-fluid-dynamics/what-is-cfd-computational-fluid-dynamics/`.

[9] J. Blazek, *Computational Fluid Dynamics: Principles and Applications (Second Edition)*. Oxford: Elsevier, 2005.

[10] D. Wilcox, *Turbulence Modeling for CFD (Third Edition)*. DCW Industries, Inc, 2006.

[11] J. D. Ali Motagamwala, “Microkinetic modeling: A tool for rational catalyst design,” *ACSPublications, Vol 121, Iss 2*, 2020.

[12] Geunsu Bae, et al., “Quantification of active site density and turnover frequency: From single-atom metal to nanoparticle electrocatalysts,” *ACSPublication, Vol 1, Iss 5*, 2021.

[13] *COMSOL Reference Manual: The Transport of Diluted Species Interface*. Accessed: 2026-03-16 , `https://doc.comsol.com/6.3/doc/com.comsol.help.cfd/cfd_ug_chemsptrans.11.006.html`.

[14] F. F. Nicoud, “Subgrid-scale stress modelling based on the square of the velocity gradient tensor,” *Flow,Turbulence and Combustion*, 1999.

[15] A. Goswami, et al., “High-throughput design of catalytic materials for nox reduction from aircraft emissions,” *Manuscript under review*, 2026.

[16] I.B. Celik, U. Ghia, et al., “Procedure for estimation and reporting of uncertainty due to discretization in cfd applications available,” *Journal of Fluids Engineering*, 2008.

[17] A. Volk, U. Ghia, C. Stoltz, “Effect of grid type and refinement method on cfd-dem solution trend with grid size,” *Powder Technology*, 2017.

[18] M. Turner, “Multistage turbine simulations with vortex–blade interaction,” *J. Turbomach. Oct 1996, 118(4): 643-653*, 1996.

A

Appendix

In this section, relevant figures, tables, and scripts that were not included in the main text, are presented.

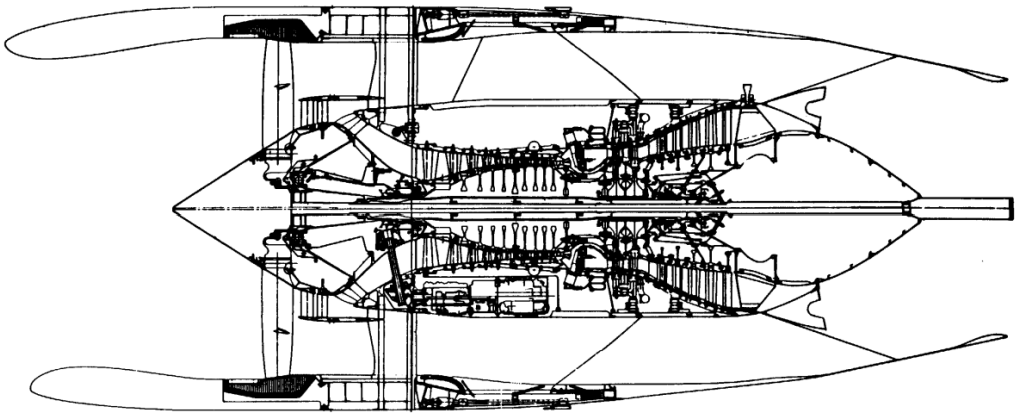

Figure A.1: Schematic of the E^3 engine from "Energy efficient engine - flight propulsion system final design and analysis" [2]

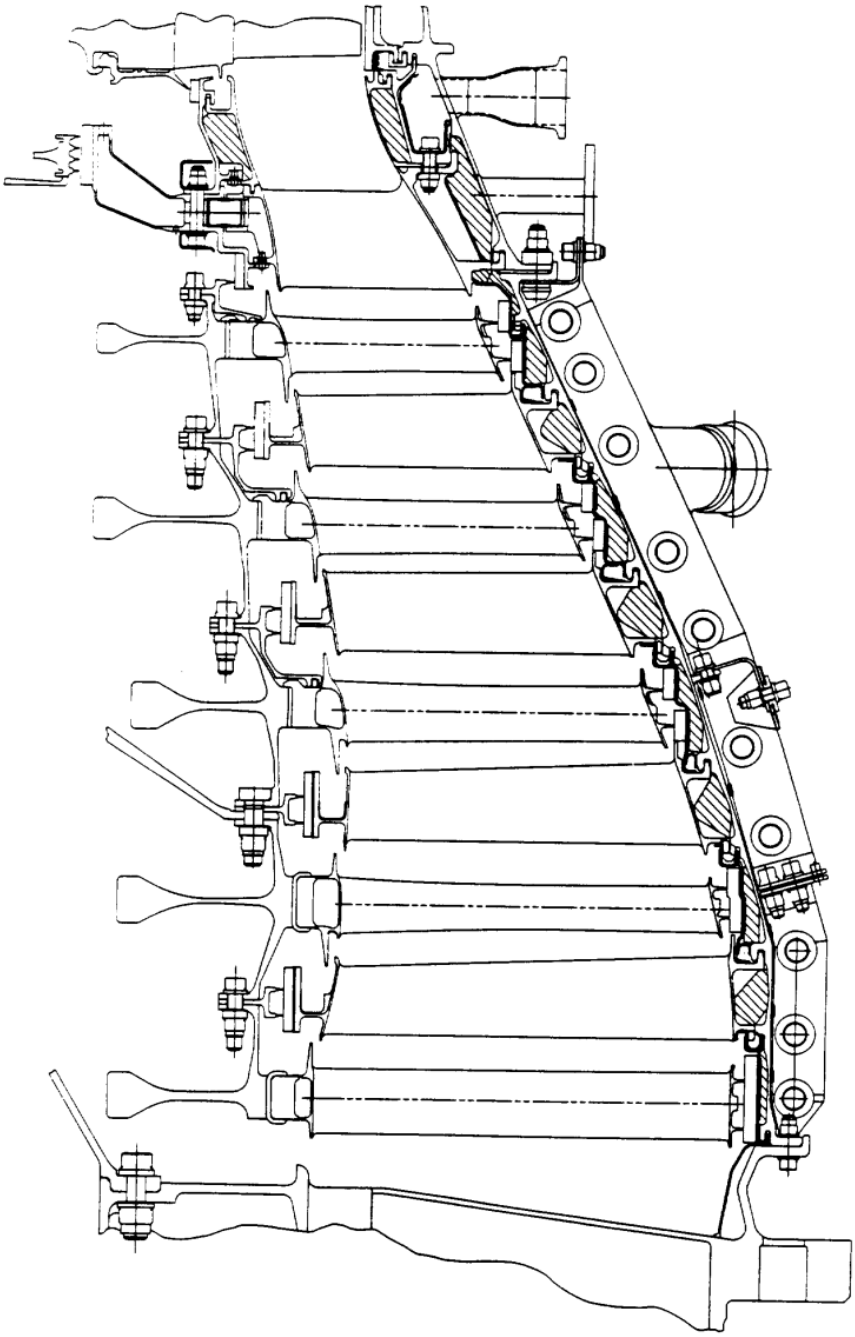

Figure A.2: Schematic of the E^3 LPT from "Energy efficient engine - flight propulsion system final design and analysis" [2]

Figure A.3: 3D geometry in blender quad mesh (viewed from the inlet)

radial/[Rcasing - Rhub]	P [Pa]	T [K]	U (axial) [m/s]	V (radial) [m/s]	W (azimuthal) [m/s]	X O2	X H2O	X CO	X CO2	X N2
0.06667	8.17455E+05	1186.98	141.06	32.70	-122.92	0.136388	0.044114	0.000000	0.047594	0.771903
0.10000	8.18094E+05	1184.73	147.41	34.37	-124.95	0.136893	0.043650	0.000000	0.047265	0.772192
0.13333	8.19831E+05	1182.33	154.88	35.72	-128.28	0.137864	0.043331	0.000000	0.046752	0.772233
0.16667	8.20287E+05	1176.42	165.29	35.24	-129.75	0.138841	0.042637	0.000000	0.046001	0.772521
0.20000	8.22095E+05	1171.17	170.30	37.31	-133.69	0.140065	0.041900	0.000000	0.045200	0.772834
0.23333	8.23712E+05	1166.62	169.07	43.75	-132.34	0.140926	0.041381	0.000000	0.044632	0.773060
0.26667	8.26952E+05	1163.47	171.65	42.70	-135.68	0.141808	0.040847	0.000000	0.044045	0.773299
0.30000	8.28091E+05	1159.98	172.33	45.34	-137.91	0.142540	0.040407	0.000000	0.043561	0.773492
0.33333	8.30311E+05	1156.27	173.00	46.61	-139.37	0.143120	0.040058	0.000000	0.043168	0.773654
0.36667	8.30812E+05	1148.58	171.81	49.12	-140.06	0.144067	0.039485	0.000000	0.042530	0.773918
0.40000	8.31525E+05	1140.33	176.12	52.89	-141.57	0.145038	0.038896	0.000000	0.041876	0.774188
0.43333	8.30988E+05	1134.78	177.14	52.70	-148.03	0.145499	0.038613	0.000000	0.041564	0.774324
0.46667	8.30935E+05	1126.00	178.71	56.88	-147.81	0.146417	0.038055	0.000000	0.040954	0.774575
0.50000	8.29720E+05	1117.89	176.97	62.31	-143.71	0.147269	0.037541	0.000000	0.040378	0.774812
0.53333	8.31168E+05	1106.94	177.95	57.72	-146.79	0.148381	0.036869	0.000000	0.039620	0.775129
0.56667	8.28539E+05	1097.32	177.18	57.38	-147.94	0.149365	0.036275	0.000000	0.038955	0.775405
0.60000	8.28529E+05	1087.92	178.31	54.02	-145.35	0.150499	0.035588	0.000000	0.038202	0.775712
0.63333	8.29934E+05	1082.96	171.64	53.36	-143.33	0.151068	0.035240	0.000000	0.037818	0.775874
0.66667	8.28959E+05	1072.29	167.80	56.69	-144.14	0.152275	0.034509	0.000000	0.037006	0.776209
0.70000	8.31071E+05	1063.51	164.77	57.39	-145.46	0.153357	0.033856	0.000000	0.036286	0.776502
0.73333	8.28307E+05	1049.10	164.01	59.18	-148.19	0.155081	0.032819	0.000000	0.035148	0.776954
0.76667	8.28272E+05	1038.22	167.10	62.87	-149.13	0.156906	0.031731	0.000000	0.033973	0.777390
0.80000	8.26049E+05	1030.40	172.93	63.93	-152.85	0.158078	0.031033	0.000000	0.033220	0.777669
0.83333	8.27975E+05	1027.31	173.38	72.97	-155.11	0.158559	0.030746	0.000000	0.032912	0.777783
0.86667	8.26757E+05	1025.69	165.15	72.95	-167.45	0.158448	0.030809	0.000000	0.032967	0.777776
0.90000	8.25936E+05	1029.94	159.51	77.85	-188.96	0.158060	0.031033	0.000000	0.033199	0.777708
0.93333	8.25144E+05	1040.90	159.34	77.59	-205.86	0.157028	0.031639	0.000000	0.033843	0.777490
0.96667	8.25764E+05	1049.40	160.71	82.88	-215.32	0.156472	0.031966	0.000000	0.034190	0.777372

Figure A.4: HPT outlet excel sheet data

```
$ sbatchrun.sh ●
Ubuntu > home > matia > 3dagain > $ sbatchrun.sh
1  #!/bin/bash -l
2  #SBATCH -A [redacted]
3  #SBATCH -J TOF_ramp
4  #SBATCH -t 7-00:00:00
5  #SBATCH --ntasks-per-node=1
6  #SBATCH --cpus-per-task=64
7  #SBATCH --nodes=1
8  #SBATCH --exclusive
9
10 module load COMSOL/6.3.0.290
11
12 INPUTFILE="3dagain1.mph"
13 OUTPUTFILE=${INPUTFILE%.mph}.out
14 BATCHLOG="${INPUTFILE%.mph}.log"
15 RDIR="/cephyr/NOBACKUP/groups/stenlid-lab_vera/AntoMat/comsol_recovery"
16
17 env > env.log
18
19 comsol batch -mpibootstrap slurm -inputfile ${INPUTFILE} -outputfile ${OUTPUTFILE} -batchlog ${BATCHLOG} -alivetime 15 -mpidebug 10
20
```

Figure A.5: Example of bash script used for running COMSOL on Vera

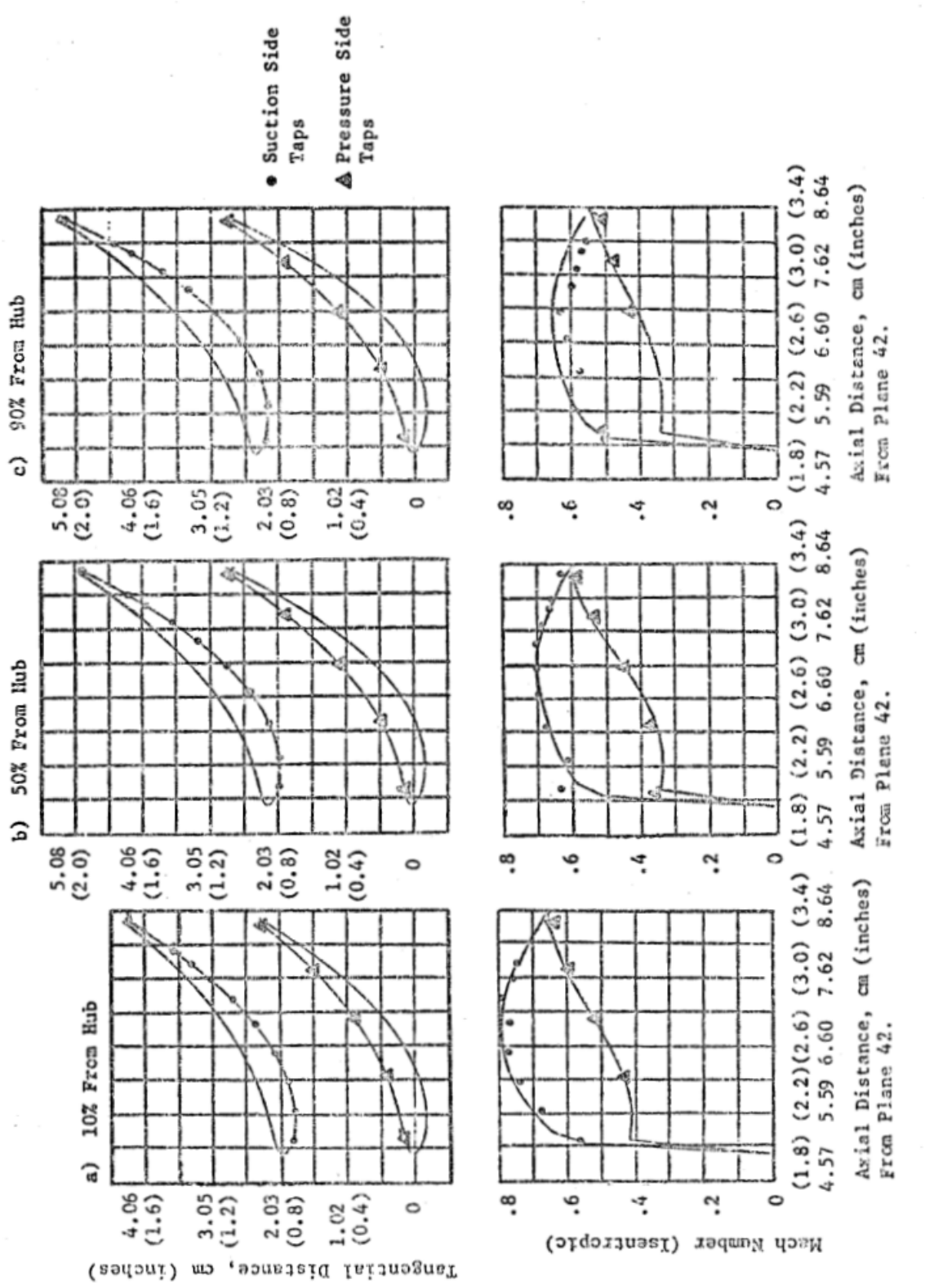

Figure A.6: Isentropic Mach Number distribution around each stator from the E^3 LPT performance report [1] calculated from static pressure taps

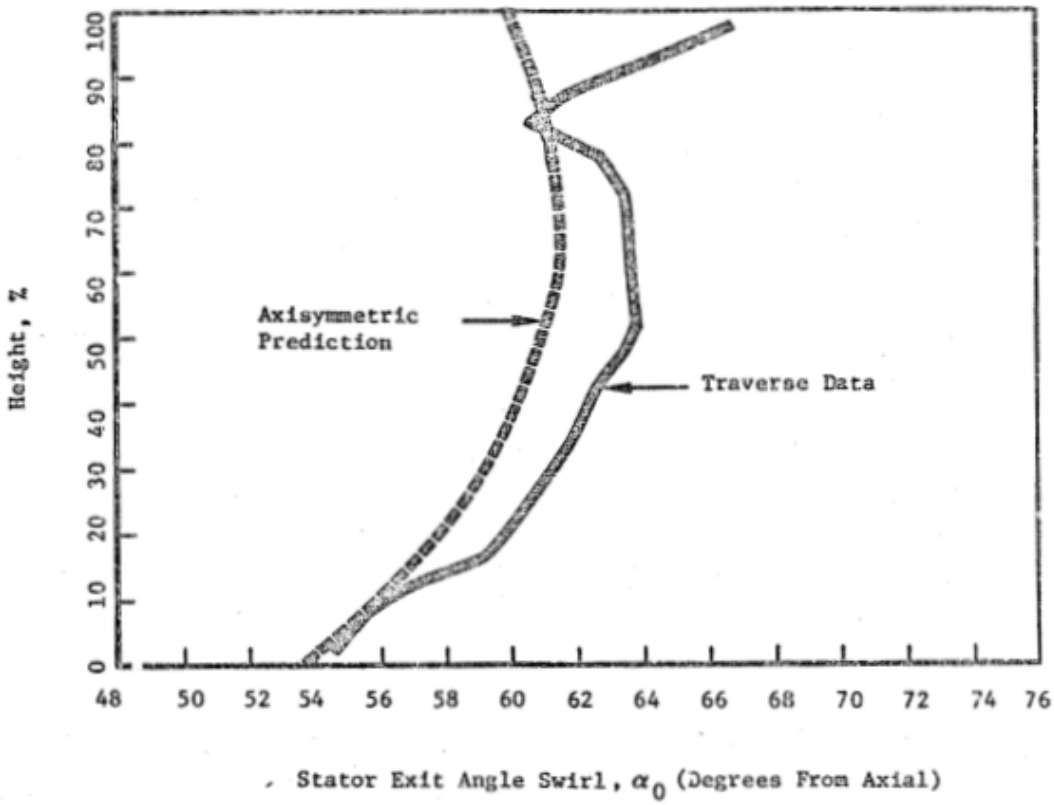

Figure 89. Block II Configuration 1a Exit Survey-Swirl Vs. % Height

130

Figure A.7: Outlet swirl angle after the first stator row from the E^3 LPT performance report [1]

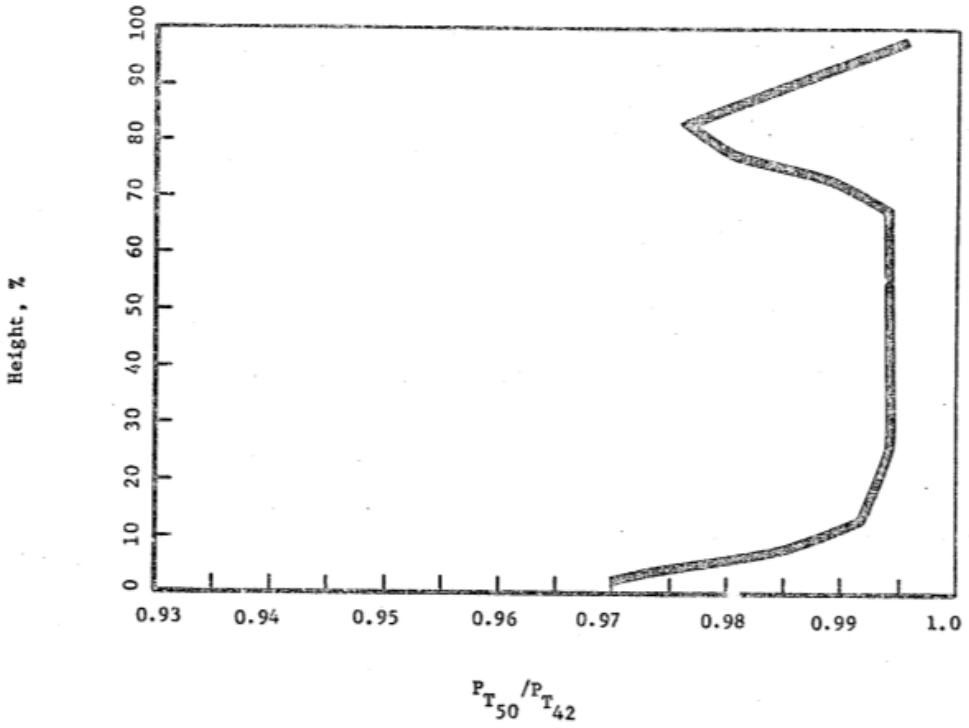

Figure 87. Block II Configuration 1a, Exit Survey-$P_{T_{50}}/P_{T_{42}}$ Vs. % Height.

128

Figure A.8: Total pressure ratio over the first stator row from the E^3 LPT performance report [1]

DEPARTMENT OF MECHANICAL ENGINEERING
CHALMERS UNIVERSITY OF TECHNOLOGY
Gothenburg, Sweden
www.chalmers.se

CHALMERS
UNIVERSITY OF TECHNOLOGY